














Higher-Order Analysis of Three-Dimensional Anisotropy in Imbalanced Alfvénic Turbulence

NIKOS SIOULAS ¹, THEMISTOCLES ZIKOPOULOS ², CHEN SHI ³, MARCO VELLI ³, TREVOR BOWEN ⁴,
ALFRED MALLET ⁴, LUCA SORRISO-VALVO ⁵, ANDREA VERDINI ⁶, B. D. G. CHANDRAN ⁷,
MIHAILO M. MARTINOVIĆ ⁸, S. S. CERRI ⁹, NOOSHIN DAVIS ⁷ AND CORINA DUNN ⁴

¹*Department of Earth, Planetary, and Space Sciences, University of California, Los Angeles, CA, USA*

²*Department of Physics, Aristotle University of Thessaloniki, GR-52124 Thessaloniki, Greece*

³*Department of Earth, Planetary, and Space Sciences, University of California, Los Angeles, CA, USA*

⁴*Space Sciences Laboratory, University of California, Berkeley, CA 94720-7450, USA*

⁵*Institute for Plasma Science and Technology (ISTP), CNR, Bari, Italy**

⁶*Università di Firenze, Dipartimento di Fisica e Astronomia, Firenze, Italy*

⁷*Space Science Center and Department of Physics, University of New Hampshire, Durham, NH 03824, USA*

⁸*Lunar and Planetary Laboratory, University of Arizona, Tucson, AZ 85721, USA*

⁹*Université Côte d’Azur, Observatoire de la Côte d’Azur, CNRS, Laboratoire Lagrange, Bd de l’Observatoire, CS 34229, 06304 Nice5cedex 4, France*

ABSTRACT

In-situ observations of imbalanced solar wind turbulence are employed to evaluate the core assumptions and higher-order scaling predictions of MHD turbulence models grounded in the principles of “Critical Balance” (CB) and “Scale-Dependent Dynamic Alignment” (SDDA).

Our results indicate that, at the energy injection scales, both outgoing and ingoing Alfvénic fluctuations undergo a weak energy cascade, $\chi_\lambda^\pm < 1$, where $\chi_\lambda^\pm \equiv \tau_A^\pm / \tau_{nl}^\pm$, the ratio of linear to non-linear timescales. Simultaneously, a tightening of SDDA is observed across this range. While the outgoing waves remain in a weak cascade state throughout the inertial range, $\chi_\lambda^+ \approx 0.2$, the ingoing waves transition to a strong cascade, $\chi_\lambda^- > 1$, at $\lambda \approx 3 \times 10^4 d_i$. This transition, however, is accompanied by spectral scalings that diverge from the expected canonical behavior marking the shift from weak to strong turbulence - a discrepancy we attribute to the effects of “anomalous coherence”. The domain canonically identified as the inertial range consists of two distinct sub-inertial segments. At $\lambda \gtrsim 100 d_i$, the “average” eddy assumes a field-aligned tube topology, with SDDA signatures being weak and largely restricted to the highest amplitude fluctuations. The scaling exponents ζ_n of the n -th order conditional structure functions, perpendicular to both the local mean field and the fluctuation direction, conform to the analytical models of Chandran et al. (2015) and Mallet & Schekochihin (2017), indicating “multifractal” statistics and strong intermittency; the scaling in the parallel and displacement (i.e., fluctuation direction) components is more concave than theoretically predicted. We argue that the statistics of this range could be contaminated by expansion effects. Below $\lambda \approx 100 d_i$, eddies display increasing anisotropy, evolving into structures resembling thin current sheets. Concurrently, ζ_n scales linearly with order, signaling a transition towards “monofractal” statistics. At $\lambda \approx 8 d_i$, the increase in aspect ratio ceases, and the eddies transition to a quasi-isotropic state. This shift might be a signature of the tearing instability, potentially leading to reconnection of the thin current sheets, or it could result from turbulent energy being channeled into an ion-cyclotron wave spectrum, consistent with the “helicity barrier” effect.

Our analysis employs 5-point structure functions, which are shown to be more effective than the traditional 2-point approach in accurately capturing the steep scaling behaviors observed at smaller spatial scales.

Keywords: Magnetohydrodynamics(MHD); Solar Wind; Plasmas; Turbulence; Waves

1. INTRODUCTION

Propelled by the internal dynamics of the Sun, the solar wind expands spherically within the heliosphere, transporting a wide spectrum of magnetic field and plasma fluctuations (Bruno & Carbone 2013). Given that fluctuations are predominantly weakly compressive (Tu & Marsch 1995), their dynamics are often analyzed within the framework of incompressible magnetohydrodynamic (MHD) theory (Biskamp 2003; Matthaeus & Velli 2011). The Elsässer (1950) form of the ideal incompressible MHD equations is given by

$$\frac{\partial \delta \mathbf{z}^\pm}{\partial t} \mp (\mathbf{V}_A \cdot \nabla) \delta \mathbf{z}^\pm = -(\delta \mathbf{z}^\mp \cdot \nabla) \delta \mathbf{z}^\pm - \frac{\nabla p}{\rho_0}, \quad (1)$$

where the Elsässer variables, $\delta \mathbf{z}^\pm = \delta \mathbf{v} \pm \delta \mathbf{b} / \sqrt{4\pi\rho}$, represent eigenfunctions of Alfvén (1942) waves propagating (anti)parallel to the background magnetic field (\mathbf{B}_0) at the Alfvén speed, $\mathbf{V}_A = \mathbf{B}_0 / \sqrt{4\pi\rho}$. The total energy $E_t = E^+ + E^-$, and cross-helicity $H_c = E^+ - E^-$, expressed in terms of the energy associated with fluctuations in \mathbf{z}^\pm , $E^\pm = \langle |\delta \mathbf{z}^\pm|^2 \rangle / 4$ are ideal (i.e., with zero viscosity and resistivity) invariants of the incompressible MHD equations. Their ratio defines the normalized cross helicity $\sigma_c = H_c / E_t$. When the energy fluxes, denoted as ϵ^\pm , in wave packets traveling in opposite directions differ, indicated by $\epsilon^+ / \epsilon^- \neq 1$, turbulence is termed as *imbalanced*, $\sigma_c \neq 0$. The nonlinearities, as highlighted by the first term on the right-hand side of Equation 1, arise from collisions between oscillation modes with opposite signs of cross-helicity (i.e. between $\delta \mathbf{z}^+$ and $\delta \mathbf{z}^-$). These inertial, or energy-conserving, interactions lead to the fragmentation of the wavepackets and drive energies of E^+ and E^- towards smaller perpendicular scales, at which point energy is converted into heat through dissipation (Iroshnikov 1963; Kraichnan 1965), henceforth referred to as IK. The turbulent cascade is strongly anisotropic and results in the formation of structures characterized by $\ell_{\parallel} \gg \lambda$, with $\ell_{\parallel} \sim 1/k_{\parallel}$ and $\lambda \sim 1/k_{\perp}$ representing the correlation lengths along and perpendicular to the background mag-

netic field¹, respectively (Montgomery & Turner 1981; Shebalin et al. 1983; Grappin 1986). The effectiveness of the collisions hinges on two critical timescales: the time it takes for a turbulent perturbation of size λ to break up nonlinearly $\tau_{nl}^\pm \sim \lambda / \delta z^\mp$ and the linear propagation (or collision) time $\tau_A^\pm = \ell_{\parallel}^\pm / V_A$. The ratio of these timescales defines the nonlinearity parameter, $\chi^\pm \equiv \tau_A^\pm / \tau_{nl}^\pm \sim (\ell_{\parallel}^\pm / \lambda) (\delta z_{\lambda}^\pm / V_A)$.²

In the limit of weak, turbulence, $\chi \ll 1$, energy transfer to smaller scales occurs fractionally upon each collision, with weak nonlinear effects accumulating over timescales significantly longer than the wave period. Under the assumption that collisions accumulate in a manner akin to a standard random walk, approximately $N \sim 1/\chi^2$ collisions are necessary to fully cascade the energy at a given scale. Dimensional analysis (Ng & Bhattacharjee 1996) and the formal application of weak perturbative theory (Galtier et al. 2000) both predict an inertial range spectrum scaling as $E \propto k_{\perp}^{-2}$.

An initial state of globally weak turbulence is often unstable, and the intrinsic anisotropy of the energy cascade inevitably develops smaller perpendicular scales that are strongly turbulent with nonlinear effects present at the leading order. The case of strong turbulence was addressed by Higdon (1984) and Goldreich & Sridhar (1995), hereafter GS95. GS95 expanded upon the idea that fluctuations in any two planes perpendicular to the mean field can remain correlated only if an Alfvén wave can propagate between them in less time than their perpendicular decorrelation time (see also, Maron & Goldreich 2001; Schekochihin et al. 2009a). This leads to the implication that the dynamics of the inertial range in incompressible MHD turbulence are governed by wavevector modes in a ‘‘critical balance’’ (CB) state, i.e., characterized by a near-equal balance between the two dynamically important timescales, essentially achieving $\chi \sim 1$. Under the assumption of negligible cross helicity, which suggests identical statisti-

¹ In assessing the dominant scale of the background magnetic field, two methodologies are predominantly employed, utilizing the global and local frames (Cho & Vishniac 2000; Maron & Goldreich 2001). For a detailed exploration of the consequences associated with defining the magnetic field either globally, thereby \mathbf{B}_0 , or locally, denoted as \mathbf{B}_{ℓ} , interested readers are encouraged to refer to (Chen et al. 2011; Matthaeus et al. 2012; Gerick et al. 2017).

² We assumed here, implicitly, that the cascade is local in k_{\perp} . However, it’s important to note that this condition may not hold in cases of strongly imbalanced turbulence (Schekochihin 2022). This point is further discussed in Section 6.

* Space and Plasma Physics, School of Electrical Engineering and Computer Science, KTH Royal Institute of Technology, Stockholm, Sweden

cal properties for counterpropagating wavepackets, this implies that the parallel and perpendicular wavevectors follow the scaling law $k_{\parallel} \propto k_{\perp}^{2/3}$. Consequently, the one-dimensional power spectra for total energy scale as $E(k_{\perp}) \propto k_{\perp}^{-5/3}$ and $E(k_{\parallel}) \propto k_{\parallel}^{-2}$, across and along the local magnetic field, \mathbf{B}_{ℓ} , respectively.

The GS95 model is directly applicable to the Reduced MHD approximation (RMHD), where the background magnetic field \mathbf{B}_0 is significantly stronger than the fluctuating amplitudes (Kadomtsev & Pogutse 1967; Strauss 1976; Oughton et al. 2017). The latter are restricted to a plane orthogonal to \mathbf{B}_0 . Despite $\delta b_{\perp} \ll \mathbf{B}_0$, nonlinear effects are retained at the leading order. This is achieved by excluding all high-frequency fluctuations $\tau_a \leq \tau_{nl}$. Consequently, fluctuations within the RMHD approximation inherently satisfy the condition $\chi \geq 1$ (Oughton & Matthaeus 2020). In this case, nonlinear interactions along the mean field may be completely neglected, allowing the nonlinear evolution to adhere to the 2D incompressible MHD equations in planes orthogonal to \mathbf{B}_0 ³.

While the core principle of the GS95 model, namely CB, was shown to be consistent with numerical simulations of homogeneous, (in)compressible MHD turbulence, the inertial range scaling perpendicular to \mathbf{B}_{ℓ} was observed to be closer to $-3/2$ (Maron & Goldreich 2001; Müller et al. 2003; Müller & Grappin 2005)⁴. Additionally, numerical simulations revealed a tendency for magnetic and velocity fluctuations in the field-perpendicular plane to align with each other within a small, scale-dependent angle (Beresnyak & Lazarian 2006).

To reconcile the noted discrepancy, Boldyrev (2005, 2006), henceforth B06, proposed a phenomenological model linking the emergence of local imbalance (Dobrowolny et al. 1980; Matthaeus et al. 2008) with the scale-dependent dynamic alignment (SDDA) in the polarizations of $\delta \mathbf{b}_{\perp}$ and $\delta \mathbf{v}_{\perp}$, towards smaller scales, $\theta_{\perp}^{ub} \sim \delta b/v_A \propto \lambda^{1/4}$. Drawing on geometrical considerations, B06 suggests that the observed increase in alignment at smaller scales is linked to both a depletion of nonlinearities and simultaneous development of local anisotropy in the plane perpendicular to \mathbf{B}_{ℓ} . In this framework turbulent eddies are identified as 3D-anisotropic structures, characterized by $\ell_{\parallel} \gg \xi \gg \lambda$, where, $\lambda/\xi \sim \sin \theta_{\perp}^{ub}$. Here, ξ represents the coherence

length in the direction of $\delta \mathbf{b}$. B06 predicts three distinct scaling laws in the inertial range: $E(k_{\xi}) \propto k_{\xi}^{-5/3}$, $E(k_{\lambda}) \propto k_{\lambda}^{-3/2}$, and $E(k_{\ell_{\parallel}}) \propto k_{\ell_{\parallel}}^{-2}$. The B06 model has been subject to criticism by Beresnyak (2011), on the basis that it conflicts with the rescaling symmetry intrinsic to the RMHD equations.

The concept of SDDA received further refinement in the work of Chandran et al. (2015), hereinafter referred to as CSM15. In their interpretation, alignment emerges as an intermittency effect, resulting from the mutual shearing of Elsässer fields during the imbalanced collisions ($\delta z^{\pm} \gg \delta z^{\mp}$) of counterpropagating wave packets. Furthermore, Mallet & Schekochihin (2017), subsequently referred to as MS17, formulated a statistical model for three-dimensional 3D anisotropic, intermittent Alfvénic turbulence. Both models integrate the principles of CB and SDDA, preserving the scale invariance characteristic of RMHD. With the incorporation of SDDA, the nonlinear timescale is defined as $\tau_{nl}^{\pm} \sim \lambda/(\delta z^{\mp} \sin \theta^z)$, wherein θ^z denotes the angle between the fluctuations of the Elsässer variables in the plane perpendicular to the magnetic field, δz_{\perp}^{\pm} . MS17 extends predictions for 3D anisotropic higher-order scaling that are consistent with the second-order moment scaling proposed by B06.

The aforementioned theoretical models focus on the dynamics of small amplitude (toroidal) Alfvén modes, neglecting potential couplings with compressive fluctuations (e.g., Cho & Lazarian 2003; Chandran 2005, 2018), within the context of globally *balanced* turbulence. In contrast, solar wind turbulence typically displays a predominance in the flux of outwardly propagating fluctuations over inwardly directed ones (Roberts et al. 1987; D’Amicis et al. 2021). In addition, the predominant fluctuations in the solar wind are consistent with large amplitude ($\delta \mathbf{b} \sim \mathbf{B}_0$) Alfvén waves. These waves are not purely transverse to \mathbf{B}_0 but exhibit spherical polarization, meaning the magnetic field vector traces a sphere of constant radius $|\mathbf{B}_0 + \delta \mathbf{b}| = \text{const.}$ (Barnes & Hollweg 1974; Bruno et al. 2001; Matteini et al. 2014). Furthermore, a non-negligible fraction of compressive fluctuations is observed (Yao et al. 2011; Howes et al. 2012; Klein et al. 2012). Finally, the dynamics of the solar wind are influenced not just by the mean field direction, but also by the radial axis along which the solar wind expands (Völk & Aplers 1973). This aspect has been illuminated by numerical simulations using the Expanding Box Model (EBM) (Grappin et al. 1993; Grappin & Velli 1996), which demonstrate that expansion preferentially reduces the radial component of the magnetic field across all scales, confining fluctuations to a plane orthogonal to the radial direction (Dong et al. 2014). Given

³ Note, however, that the RMHD approximation encompasses essential elements of the physics of three-dimensional incompressible MHD (Dmitruk et al. 2005; Oughton et al. 2017)

⁴ Recent higher resolution simulations further support this finding (Perez et al. 2012; Verdini & Grappin 2015; Mallet et al. 2016; Dong et al. 2022; Shi et al. 2023)

these considerations, the extent to which phenomenological models of homogeneous, Alfvénic turbulence can accurately capture the unique characteristics of the solar wind remains an active area of debate (Bowen et al. 2021).

In this investigation, we endeavor to evaluate the consistency of the homogeneous models of balanced MHD turbulence proposed by CSM15 and MS17 against in-situ observations sampled during the first perihelion (E1) of the Parker Solar Probe mission, (PSP, Fox et al. 2016). Our primary objective is to conduct a rigorous comparison between the predicted scalings of higher-order moments in these models and the corresponding empirical observations, with a specific focus on determining the presence and measurable impact of model-specific elements, such as SDDA and CB, on the observed characteristics. Through this analysis, our aim is to not only provide deeper insights into the higher-order statistics of magnetic turbulence but also to establish a robust benchmark for the testing and refinement of theoretical models addressing imbalanced MHD turbulence in the inhomogeneous solar wind.

The structure of the remainder of the paper is as follows: Section 2 provides theoretical background on intermittency and summarizes the core principles of the CSM15 and MS17 models. Section 3 elaborates on the methodologies utilized in this analysis. Details regarding data selection and processing are outlined in Section 4. The study’s findings are presented in Section 5. A comprehensive comparison with prior theoretical, observational, and numerical studies, which contextualizes our results, is provided in Section 6. The paper concludes with a summary of the main findings in Section 7.

2. THEORETICAL BACKGROUND: INTERMITTENCY

Kolmogorov (1941) (hereafter K41), postulated that the cascade process is intricate enough for eddies to lose all memory of their past and that their properties after each cascade step can be explained by random distributions. An inertial range arises where eddies are too large for viscosity to play a significant role and too small to retain any influence from large-scale inhomogeneities. A universal probability density function (PDF), $P(\delta u, \ell)$, emerges over this range. The velocity difference between non-proximate points can be expressed as the sum of velocity differences over subintervals, justifying a plausible Gaussian distribution assumption based on the central limit theorem. The validity of this assumption hinges on two conditions: mutual independence among summands and comparable finite variances in the subin-

terval probability distributions (Feller 1968). Considering a global energy transfer rate that is independent of scale, ϵ , and utilizing the statistical moments of the PDFs called structure functions (SF^n):

$$SF_i^n(\ell) = \int_{-\infty}^{\infty} (\delta u_i)^n P(\delta u_i, \ell) d(\delta u_i), \quad (2)$$

where, δu_i denotes longitudinal velocity increments, $\delta u_i = V_i(\mathbf{r} + \ell) - V_i(\mathbf{r})$, Kolmogorov’s similarity hypothesis yields:

$$SF_i^n(\ell) \sim \epsilon^{n/3} \ell^{\zeta^{K41}(n)}, \quad (3)$$

where $\zeta^{K41}(n) = n/3$, implying global scale invariance (self-similarity) of the fluctuations.

In the case of MHD turbulence, IK introduced a phenomenological model based on the coupling of small-scale velocity and magnetic fluctuations by the large-scale background magnetic field, \mathbf{B}_0 . Compared to K41, the spectral transfer is reduced by a factor of τ_A/τ_{nl} owing to the limited strength of the interaction exhibited by Alfvén waves. Also in this case the scaling exponents of SF^n are expected to scale linearly with order n , i.e., $\zeta^{IK}(n) = n/4$.

However, it was soon realized experimentally that PDFs of fluctuations in hydrodynamic (HD) and MHD turbulence tend to display increasingly non-Gaussian behavior at progressively smaller scales (Batchelor et al. 1949; Burlaga 1991; Sorriso-Valvo et al. 1999). Additionally, it has been noted that the spatial inhomogeneity of energy dissipation is expected to alter the scaling exponents of field increments with respect to length scales ℓ (Oboukhov 1962; Kolmogorov 1962). Specifically, if the energy transfer rate from larger to smaller eddies statistically varies with ℓ , then the dissipation rate ϵ in Equation 3 should be substituted with ϵ_ℓ (Lanford & Lifshitz 1959):

$$SF_i^n(\ell) \sim \langle \epsilon_\ell^{n/3} \rangle \ell^{n/3}. \quad (4)$$

Expressing $\epsilon_\ell^{n/3}$ through a scaling relation with ℓ , we find $\langle \epsilon_\ell^{n/3} \rangle \sim \ell^{\tau_n/3}$, leading to

$$SF_i^n(\ell) \sim \ell^{\zeta_n}, \quad (5)$$

where, $\zeta_n = n/3 + \tau_n/3$ is generally a nonlinear function of n . When analyzing the scaling exponents ζ_n of the structure functions, deviations from linear scaling, indicate a violation of global scale invariance, which implies a process characterized by “multifractal” statistics and intermittency, i.e., the concentration of the energy into smaller volumes of space at smaller scales (Frisch

1995). Several authors have put forward theoretical arguments to account for the intermittency effect (Gurland & Tripathi 1971; Frisch et al. 1978; She & Leveque 1994; Grauer et al. 1994; Politano & Pouquet 1995; Ruzmaikin et al. 1995; Horbury & Balogh 1997a; Müller & Biskamp 2000; Boldyrev 2002).

Chandran, Schekochihin, and Mallet Chandran et al. (2015) (henceforth CSM15) introduced a model founded on collisions of Alfvénic wavepackets making a series of plausible assumptions regarding the dynamics and statistics of RMHD turbulence. In formulating an analytical model, they proposed two primary types of non-linear interactions. The first involves occasional “balanced” interactions, $\delta z^- \approx \delta z^+$, where the amplitude of the wavepackets is reduced by a factor of $0 \leq \beta \leq 1$, yet their length scale remains unchanged. Consequently, the amplitude of a fluctuation at scale λ resulting from such balanced collisions can be expressed as follows:

$$\delta z_\lambda^\pm = \delta \bar{z} \beta^q. \quad (6)$$

Here, $\delta \bar{z}$ is the initial fluctuation amplitude at the injection scale L , and q is the number of balanced collisions expected as the fluctuation evolves from scale L to λ . The value of q is presumed to follow a Poisson distribution:

$$P(q) = \frac{e^{-\mu} \mu^q}{q!}, \quad (7)$$

where μ is the scale-dependent mean value of q . The “typical” fluctuation amplitude that best characterizes the bulk of the volume is

$$\delta z_\lambda^* = \delta \bar{z} \beta^\mu. \quad (8)$$

On the contrary, for “imbalanced”, $\delta z^\pm \gg \delta z^\mp$, collisions, the amplitudes of the fluctuations remain constant while the sub-dominant field is sheared into alignment and its perpendicular scale λ reduces. Assuming that the most intense coherent structures in MHD turbulence –specifically, those with $q = 0$ – are 3D anisotropic current sheets with a volume filling factor $f_{cs} \propto \lambda$, this leads to a straightforward relation for the scaling exponents:

$$\zeta^{CSM15}(n) = 1 - \beta^n. \quad (9)$$

By focusing solely on the scenario of zero cross helicity, CSM15 deduce a value for $\beta \approx 0.691$. This implies that $\zeta_n \rightarrow 1$ as $n \rightarrow \infty$.

Furthermore, the model offers predictions for the alignment angles between the perpendicular components of velocity-magnetic and/or Elsässer field fluctuations defined in various ways. Conventionally, the alignment is estimated as

$$\sin(\theta_\perp^{ub}) = \left\langle \frac{|\delta \mathbf{b}_\perp \times \delta \mathbf{v}_\perp|}{|\delta \mathbf{b}_\perp| |\delta \mathbf{v}_\perp|} \right\rangle. \quad (10)$$

A similar expression can be formulated for the angle between Elsässer field fluctuations, δz_\perp^\pm , which relates to the residual of magnetic over kinetic energy, usually studied through the lens of the normalized residual energy :

$$\sigma_r = \frac{\langle \delta v_\perp^2 \rangle - \langle \delta b_\perp^2 \rangle}{\langle \delta v_\perp^2 \rangle + \langle \delta b_\perp^2 \rangle}. \quad (11)$$

Similarly, the Elsässer imbalance is assessed by comparing the relative energy in inwardly and outwardly propagating Alfvén waves (Velli et al. 1991; Velli 1993):

$$\sigma_c = \frac{2\langle \delta \mathbf{v}_\perp \cdot \delta \mathbf{b}_\perp \rangle}{\langle \delta v_\perp^2 \rangle + \langle \delta b_\perp^2 \rangle} \quad (12)$$

Observations from numerical simulations showed little to no scaling of alignment angles as defined in Equation 10, (Beresnyak & Lazarian 2009). However, an alternate definition of these angles, achieved by separately averaging the numerator and denominator –referred to as polarization intermittency– was proposed by (Beresnyak & Lazarian 2006):

$$\sin(\tilde{\theta}_\perp^{ub}) = \frac{\langle |\delta \mathbf{b}_\perp \times \delta \mathbf{v}_\perp| \rangle}{\langle |\delta \mathbf{b}_\perp| |\delta \mathbf{v}_\perp| \rangle}. \quad (13)$$

In a similar manner, we can define the angle between the two Elsässer fields as $\tilde{\theta}_\perp^z$. The model by CSM15 predicts $\tilde{\theta}_\perp^{ub} \propto \lambda^{0.21}$ and $\tilde{\theta}_\perp^z \propto \lambda^{0.10}$.

Mallet & Schekochihin (2017) (hereafter, MS17) formulated a statistical model of RMHD turbulence grounded in three principal concepts: critical balance, dynamic alignment, and intermittency. To substantiate their model, they put forth four conjectures based on physical reasoning: (a) the fluctuation amplitudes adhere to an anisotropic log-Poisson distribution (Chandran et al. 2015; Zhdankin et al. 2016); (b) the structures at small scales are 3D anisotropic with a sheet-like morphology (Boldyrev 2006; Howes 2015); (c) the scale-independence of the critical balance parameter, inclusive of dynamic alignment, within the inertial range (Mallet et al. 2015); (d) a consistent energy flux across parallel scales in the inertial range (Beresnyak 2015). The model offers predictions for scaling in the perpendicular, parallel, and fluctuation directions:

For the perpendicular direction:

$$\zeta_\lambda^{MS17}(n) = 1 - \beta^n, \quad (14)$$

for the parallel direction:

$$\zeta_{\ell_\parallel}^{MS17}(n) = 2(1 - \beta^n), \quad (15)$$

and for the fluctuation direction:

$$\zeta_{\xi}^{MS17}(n) = \frac{n(1 - \beta^n)}{n/2 + 1 - \beta^n}, \quad (16)$$

where $\beta = 1/\sqrt{2}$. A more practical discussion of the model is presented in [Schekochihin \(2022\)](#).

3. DATA ANALYSIS

To investigate and quantify the three-dimensional anisotropy of higher-order magnetic field moments, we employ a methodology proposed by [Wang et al. \(2022\)](#), which builds upon and extends the framework established in [Chen et al. \(2012\)](#).

Adhering to the approach outlined in [Chen et al. \(2012\)](#), we establish a locally-defined, scale-dependent Cartesian coordinate system, represented as $(\hat{\xi}, \hat{\lambda}, \hat{\ell}_{||})$. In this coordinate system the ‘‘parallel’’ direction, $\hat{\ell}_{||}$, is aligned with the local magnetic field, \mathbf{B}_{ℓ} , defined by:

$$\mathbf{B}_{\ell} = [\mathbf{B}(\mathbf{r} + \boldsymbol{\ell}) + \mathbf{B}(\mathbf{r})]/2, \quad (17)$$

where $\boldsymbol{\ell} = \tau(\mathbf{V}_{\ell} - \mathbf{V}_{\text{sc}})$ represents the displacement vector, where \mathbf{V}_{ℓ} and \mathbf{V}_{sc} are the local scale-dependent velocity field and the spacecraft velocity, respectively, in the RTN coordinate system ([Franz & Harper 2002](#)). Magnetic field increments are calculated using:

$$\delta\mathbf{b} = \mathbf{B}(\mathbf{r} + \boldsymbol{\ell}) - \mathbf{B}(\mathbf{r}). \quad (18)$$

The amplitude of the field increment is denoted as $\delta b = |\delta\mathbf{b}|$. The local ‘‘displacement’’ direction, $\hat{\xi}$, aligns with the unit vector of the perpendicular component of the field increment, with $\delta\mathbf{b}_{\perp}$ defined as:

$$\delta\mathbf{b}_{\perp} = \mathbf{B}_{\ell} \times (\delta\mathbf{b} \times \mathbf{B}_{\ell}). \quad (19)$$

Lastly, the ‘‘perpendicular’’ direction, $\hat{\lambda}$, is orthogonal to both $\hat{\xi}$ and $\hat{\ell}_{||}$, $\hat{\lambda} = \hat{\ell}_{||} \times \hat{\xi}$. The Cartesian system can be converted into a spherical polar coordinate system $(\ell, \theta_B, \phi_{\delta\mathbf{B}_{\perp}})$, where θ_B is the angle between \mathbf{B}_{ℓ} and $\boldsymbol{\ell}$, and $\phi_{\delta\mathbf{B}_{\perp}}$ is the angle between $\hat{\xi}$ and the projection of $\boldsymbol{\ell}$ onto the plane orthogonal to \mathbf{B}_{ℓ} .

In our analysis, we utilize the 5-point (5-point) increment method, which represents a significant advancement over the conventional 2-point (2-point) method, especially for examining turbulence statistics in sub-ion regimes ([Cerri et al. 2019](#)). A critical benefit of the 5-point method is its reduced susceptibility to large-scale spectral leakage ([Cho 2019](#)), rendering it more suitable and effective for our ensuing analysis.

For calculating 5-point structure functions, denoted as SF_5^n , a modified definition of $\delta\mathbf{b}$ is required

$$\delta\mathbf{b} = \frac{1}{\sqrt{35}} [\mathbf{B}(\mathbf{r} - 2\boldsymbol{\ell}) - 4\mathbf{B}(\mathbf{r} - \boldsymbol{\ell}) + 6\mathbf{B}(\mathbf{r}) - 4\mathbf{B}(\mathbf{r} + \boldsymbol{\ell}) + \mathbf{B}(\mathbf{r} + 2\boldsymbol{\ell})]. \quad (20)$$

Moreover, the local scale-dependent value ψ_{ℓ} of a field $\boldsymbol{\psi}$ can be computed as a weighted average using a five-point stencil:

$$\psi_{\ell} = \frac{1}{16} [\boldsymbol{\psi}(\mathbf{r} - 2\boldsymbol{\ell}) + 4\boldsymbol{\psi}(\mathbf{r} - \boldsymbol{\ell}) + 6\boldsymbol{\psi}(\mathbf{r}) + 4\boldsymbol{\psi}(\mathbf{r} + \boldsymbol{\ell}) + \boldsymbol{\psi}(\mathbf{r} + 2\boldsymbol{\ell})]. \quad (21)$$

For example, the local scale-dependent magnetic and velocity fields are represented by \mathbf{B}_{ℓ} and \mathbf{V}_{ℓ} , respectively.

The n th-order, structure functions conditioned on the pair of angles $\theta_B, \phi_{\delta\mathbf{B}_{\perp}}$, are defined as:

$$SF^n(\ell, \theta_B, \phi_{\delta\mathbf{B}_{\perp}}) = \langle (\delta B)^n | \theta_B, \phi_{\delta\mathbf{B}_{\perp}}, \ell \rangle, \quad (22)$$

The conditional average in Equation 22 was calculated over the angle bin $\omega(i-1)^{\circ} \leq \theta_B \leq \omega i^{\circ}$, $\omega(j-1)^{\circ} \leq \phi_{\delta\mathbf{B}_{\perp}} \leq \omega j^{\circ}$, where $i = 1, \dots, 9$ and $j = 1, \dots, 9$. In the following, ω takes the value of $\omega = 5$ for estimating lower-order moments and $\omega = 10$ for higher-order moments.

In the following, we focus mainly on three special cases, defining the components in

$$i = 1, \quad j = 1: \quad SF(\ell_{||})^n, \quad \text{‘‘parallel’’}, \quad (23)$$

$$i = 9, \quad j = 1: \quad SF(\xi)^n, \quad \text{‘‘displacement’’}, \quad (24)$$

$$i = 9, \quad j = 9: \quad SF(\lambda)^n, \quad \text{‘‘perpendicular’’}, \quad (25)$$

directions, where $\ell_{||} = \boldsymbol{\ell} \cdot \hat{\ell}_{||}$, $\lambda = \boldsymbol{\ell} \cdot \hat{\lambda}$, and $\xi = \boldsymbol{\ell} \cdot \hat{\xi}$.

To estimate a component structure function for the entire dataset, we adopt the methodology outlined in [Verdini et al. \(2018\)](#). For each selected interval, j , within the dataset, we compute the structure functions $SF_j^n(\ell, \theta_B, \phi_{\delta\mathbf{B}_{\perp}})$ for the three orthogonal components, as defined by Equations 23 to 25. Considering the substantial variation in the root mean square (rms) of fluctuations between intervals, normalization is a critical step prior to averaging these intervals. The normalization involves selecting a specific scale, ℓ_* , and normalizing each SF_j^n by the energy of fluctuations at that scale. We determine an appropriate ℓ_* by estimating the trace structure function $S_j^n(\ell)$ for each interval and identifying a scale range where power-law behavior is consistent across all $S_j^n(\ell)$. The fluctuation energy at scale ℓ_* is given by the value of the trace structure function $S_i(\ell_*)$.

The normalized weighted average structure function for a given magnetic field component is then calculated as follows:

$$\tilde{SF}^n(\ell, \theta_B, \phi_{\delta\mathbf{B}_\perp}) = \sum_j \frac{SF_j^n(\ell, \theta_B, \phi_{\delta\mathbf{B}_\perp})}{S_j^n(\ell_*)} W_j, \quad (26)$$

where $W_j = n_j(\ell, \theta_B, \phi_{\delta\mathbf{B}_\perp})/n(\ell, \theta_B, \phi_{\delta\mathbf{B}_\perp})$ represents the weighting factor, with $n_j(\ell, \theta_B, \phi_{\delta\mathbf{B}_\perp})$ being the total number of measurements within each bin for the interval under consideration, divided by the count in each bin for the whole data set, $n = \sum_j n_j$.

Our subsequent analysis, as discussed in Section 4, relies on these conditionally defined structure functions, utilizing data from the first perihelion of the Parker Solar Probe (PSP). Unless specified otherwise, the results in the following analysis are derived from estimating 5-point structure functions.⁵

4. DATA SET

We analyze magnetic field and particle data collected during the first perihelion of the PSP mission, covering the period from November 1 to November 11, 2018. Specifically, we analyze magnetic field measurements obtained by the FIELDS instrument (Bale et al. 2016). In particular, we make use of the SCaM data product, which combines measurements from fluxgate and search-coil magnetometers (SCM) by using frequency-dependent merging coefficients. This approach allowed us to observe the magnetic field over a frequency range ranging from direct current (DC) to 1 MHz while achieving optimal signal-to-noise ratio (Bowen et al. 2020). The FIELDS magnetometer suite is susceptible to narrow-band coherent noise stemming from the spacecraft reaction wheels, including their rotation frequencies, as well as harmonic and beat frequencies. To address potential contamination of magnetic field measurements at ion-scales by the reaction wheels, for each interval, we implement a procedure involving the identification and elimination of reaction wheel noise using the method detailed in Shankarappa et al. (2023).

Moreover, we incorporated data from the Solar Probe Cup (SPC) instrument, which is part of the Solar Wind Electrons Alphas and Protons (SWEAP) suite (Kasper et al. 2016), to estimate bulk plasma properties. We also utilized Quasi Thermal Noise (QTN) electron density measurements (Moncuquet et al. 2020; Pulupa et al. 2017). To enhance statistical robustness and expand the

Table 1. The median values for the spectral indices of the trace, parallel, perpendicular, and displacement components of the magnetic field in the ranges R_1 and R_2 . These indices are derived from the corresponding scaling indices of $SF_{5,i}^2$, utilizing the relationship $\alpha_i = -1 - \beta_i$ (Monin & Jaglom 1987). The error values provided represent the standard deviation of the mean.

| | α | $\alpha_{\ell_{\parallel}}$ | α_{λ} | α_{ξ} |
|-------|------------------|-----------------------------|--------------------|------------------|
| R_1 | -1.79 ± 0.06 | -1.97 ± 0.05 | -1.64 ± 0.04 | -1.94 ± 0.06 |
| R_2 | -1.53 ± 0.02 | -1.66 ± 0.05 | -1.49 ± 0.03 | -1.56 ± 0.08 |

sample size, the data were segmented into 12-hour intervals. These intervals were designed to overlap by 6 hours to maximize data utilization. We then conditioned the intervals based on σ_c , selecting only those with an average value of $\sigma_c(\ell_*) \geq 0.75$, where $\ell_* = 10^4 d_i$. This methodology yielded a total of 82 intervals, sampled at distances ranging from 0.166 to 0.244 au.

5. RESULTS

5.1. A Comparison of SF_5^n and SF_2^n

This section is dedicated to a comparative analysis aimed at substantiating our preference for the 5-point structure function method over the traditionally favored 2-point approach. To this end, we calculated second-order structure functions for the parallel, perpendicular, and displacement components according to Equations 23 to 25, setting $\omega = 5$. This involves estimating \mathbf{B}_ℓ and $\delta\mathbf{b}$ as per Equations 17 to 19 for SF_2^2 , and Equations 21 to 22 for SF_5^2 .

The local 2-point structure functions (circles) and 5-point structure functions (squares) averaged for the five most highly Alfvénic intervals within our dataset are illustrated in Figure 1. To highlight specific scale ranges, pink and gray shadings are employed for intervals $8-100d_i$ (labeled R_1) and $200-6000d_i$ (labeled R_2), respectively. At large scales, comparable results are obtained from both the 5-point and 2-point methods. However, a marked divergence is observed in the R_1 range. The 5-point method reveals steep scaling for parallel and displacement components, with indices $\beta_{\ell_{\parallel}} \approx \beta_{\xi} \approx 1$, aligning with wavelet-derived parallel component scaling of the same dataset reported in Sioulas et al. (2023). In contrast, the 2-point method produces a notably flatter slope.

The distinction between the two methods becomes stark at kinetic scales, highlighting the 2-point method's limitations in detecting steep scalings. This shortfall is further evident when comparing \mathbf{B} -trace wavelet structure functions using both the SF_2^2 and SF_5^2 methods; only the 5-point approach produces scalings that align

⁵ The algorithm detailed in this section, along with a package for downloading, cleaning, and processing PSP data, is readily accessible in [MHD_TurbPy](#) (Sioulas 2023).

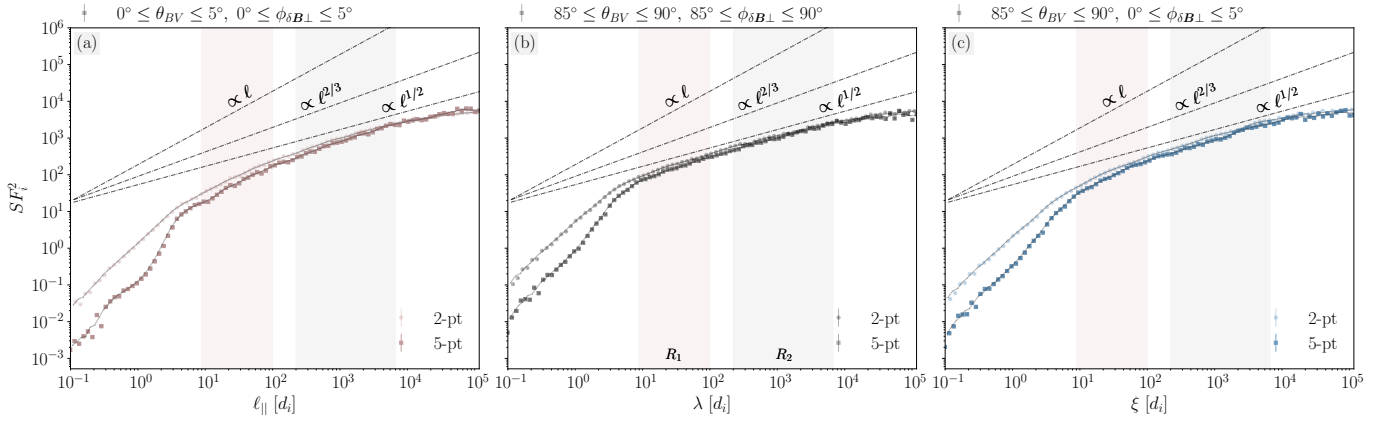


Figure 1. The local 2-point structure functions (circles) and 5-point structure functions (squares) averaged for the five most highly Alfvénic intervals within our dataset. The structure functions are displayed for the parallel, perpendicular, and displacement directions, indicated by red, black, and blue colors, respectively. Reference lines representing scalings of 1/2, 2/3, and 1 are included for comparison.

with wavelet analyses across scales from injection to kinetic (details not shown here). This inconsistency underscores potential inaccuracies when employing the 2-point method in scenarios characterized by steep scaling, as also emphasized by Cerri et al. (2019)⁶. Therefore, for our further analyses, we have chosen to rely on the 5-point method.

Across all examined intervals, the results remained qualitatively consistent. Three such intervals are illustrated in panels (g)-(h) of Figure 2. In addition to the component structure functions, these panels also illustrate the trace structure function estimated for the respective intervals. It can be observed that the perpendicular component can significantly diverge from the trace, while the latter typically shows remarkable overlap with the displacement component, with the difference becoming more pronounced towards smaller scales.

Table 4 presents the median SF_5^2 scalings estimated across the R_1 and R_2 ranges for the entire dataset.

5.2. Power \mathcal{E} wavevector anisotropy

To examine the scale-dependent three-dimensional anisotropy in our dataset, we calculated $SF_5^2(\ell)$, following the methodology outlined in Equations 23 to 25, setting $\omega = 5$. Our analysis commenced by identifying the anisotropic relationships for individual intervals, then proceeded to compute a scale-dependent median for the entire dataset, utilizing 150 logarithmically spaced bins.

Table 2. Median values of the scaling indices for wavevector anisotropies, specifically $\ell_{||} \propto \lambda^{w_{\ell_{||}}}$ and $\xi \propto \lambda^{w_{\xi}}$, and the power anisotropies $E_{\lambda}/E_{\ell_{||}} \propto \lambda^{p_{\ell_{||}}}$ and $E_{\lambda}/E_{\xi} \propto \lambda^{p_{\xi}}$. These indices were derived by applying a power-law fit to the curves obtained from individual intervals over the scale ranges R_1 and R_2 . The table presents the median values along with their associated errors, represented as the standard deviation of the mean.

| | $w_{\ell_{ }}$ | w_{ξ} | $p_{\ell_{ }}$ | p_{ξ} |
|-------|-----------------|-----------------|------------------|------------------|
| R_1 | 0.89 ± 0.06 | 0.77 ± 0.05 | -0.31 ± 0.04 | -0.30 ± 0.07 |
| R_2 | 0.86 ± 0.08 | 0.99 ± 0.06 | -0.19 ± 0.05 | -0.09 ± 0.06 |

Panels (a) and (b) of Figure 3 illustrate the anisotropic relationships $\ell_{||}(\lambda)$, and $\xi(\lambda)$, derived by equating pairs of structure functions: $SF_5^2(\lambda)$ with $SF_5^2(\ell_{||})$, and $SF_5^2(\lambda)$ with $SF_5^2(\xi)$, respectively. The aspect ratios $\ell_{||}/\lambda$ and ξ/λ are represented by gray lines in their respective panels. Panel (c) focuses on power anisotropy, illustrating the ratios $SF_5^2(\lambda)/SF_5^2(\ell_{||})$ and $SF_5^2(\lambda)/SF_5^2(\xi)$ in red and blue, respectively. The median values of the dataset’s anisotropic scalings are summarized in Table 5.2.

At large scales, our observations reveal a rough equipartition of the fluctuating energy between $SF_5^2(\lambda)$ and $SF_5^2(\ell_{||})$, with $SF_5^2(\xi)$ being slightly more energetic. The energy distribution is reflected in the wavevector anisotropy and aspect ratios, indicating that eddies tend to be slightly compressed along the fluctuation direction.

Within the R_2 range, we note that the fluctuating magnetic energy is distributed almost evenly between the perpendicular and displacement components. This observation suggests rough axisymmetry of the turbulent eddies at these scales, i.e., approximate isotropy in the plane perpendicular to \mathbf{B}_{ℓ} . The aspect ratio

⁶ A cautionary note is warranted: when comparing SF_5^2 with wavelet-derived trace structure functions for intervals observed in later PSP encounters —characterized by shallower than 1/f energy injection scale power spectra (Huang et al. 2023; Davis et al. 2023)— SF_5^2 fails to replicate the wavelet scalings. This indicates that SF_5^2 , similar to its SF_2^2 counterpart, is ineffective under conditions with scalings shallower than 1/f.

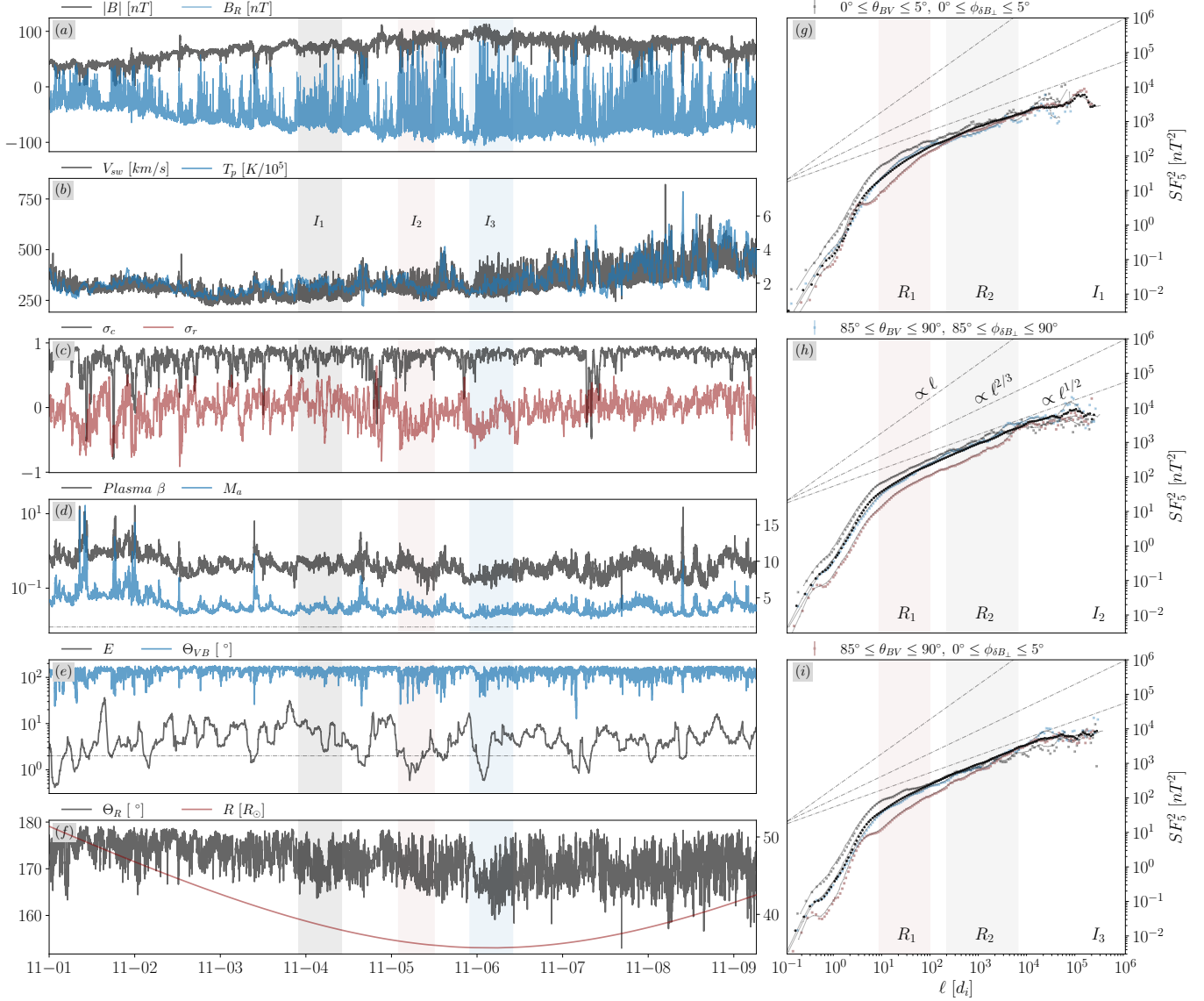


Figure 2. Overview of E1: (a) Magnetic field timeseries, radial component, B_R (blue) and magnitude, $|B|$ (black); (b) Solar wind speed, V_{sw} (black, left axis) and proton temperature, T_p (blue, right axis); (c) Normalized cross helicity, σ_c (black) and normalized residual energy, σ_r (red); (d) Plasma β (black, left axis) and Alfvénic Mach number, $M_a = V_R/|V_a|$ (blue, right axis); (e) Variance anisotropy, $E = (b_T^2 + b_V^2)/b_R^2$, where b represents the rms amplitude of fluctuations (black, left axis) and angle between the magnetic field and velocity flow, Θ_{VB} (blue); (f) Sampling angle, Θ_R , defined as the angle between \hat{R} and $\mathbf{V}_{sc} - \mathbf{V}_{sw}$ (black, left axis), and radial distance from the Sun, R (red, right axis). Additionally, three intervals denoted as I_j , $j = 1, 2, 3$ and marked with black, pink, and cyan shadings on the main figure. The corresponding 5-point structure functions of the parallel, perpendicular, and displacement directions, denoted by red, transparent black, and blue colors, respectively, are shown in panels (g)-(i). In addition, the trace structure function is shown in black circles. Reference lines representing scalings of $1/2$, $2/3$, and 1 are included for comparison.

ξ/λ is observed to be close to, yet marginally greater than, unity, displaying only a slight increase within R_2 . This trend is further emphasized by the scale-dependent power-anisotropy depicted in panel (c). In contrast, within this range, eddies exhibit elongation along \mathbf{B}_ℓ , as indicated by the ratio ℓ_{\parallel}/λ , which is greater than 1 and shows a monotonic increase towards smaller

scales. These findings collectively indicate that turbulent eddies within the R_2 range predominantly exhibit a field-aligned tube topology, consistent with the results presented in Vinogradov et al. (2023). This is visually demonstrated in Figure 4. At scales smaller than $\lambda \lesssim 100d_i$, a noticeable shift from isotropy in the plane perpendicular to \mathbf{B}_ℓ becomes evident. This shift

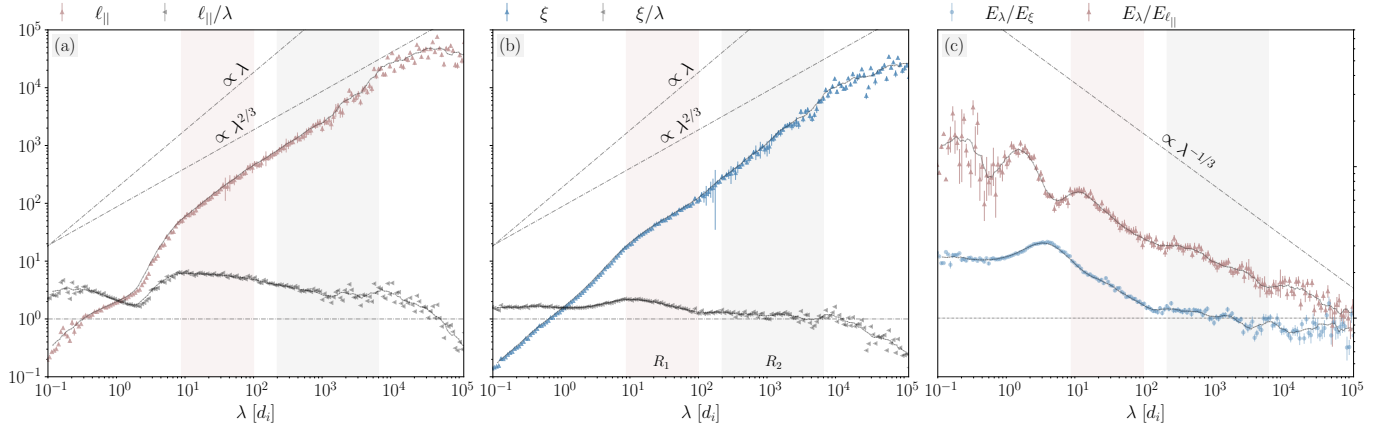


Figure 3. Wavevector anisotropy relationships: (a) $\ell_{\parallel} = \ell_{\parallel}(\lambda)$ (b) $\xi = \xi(\lambda)$, determined by equating pairs of $SF_5^2(\lambda)$ with $SF_5^2(\ell_{\parallel})$, and $SF_5^2(\lambda)$ with $SF_5^2(\xi)$, respectively. The gray lines show the aspect ratios, ℓ_{\parallel}/λ and ξ/λ plotted against λ in panels (a) and (b), respectively. For context, reference lines indicating scalings of $2/3$ and 1 are also included. Panel (c) presents power anisotropy, with $E_{\lambda}/E_{\ell_{\parallel}}$ depicted in red and E_{λ}/E_{ξ} in blue.

is highlighted by a gradual increase in the aspect ratio ξ/λ , indicating a transition of eddy structures from tube-like to ribbon-like. The evolving eddies exhibit three-dimensional anisotropy, adhering to the relationship $\ell_{\parallel} \gg \xi \gg \lambda$. This trend persists into the smaller-scale end of the R_1 range, where both power-anisotropy ratios follow a scaling of approximately $-1/3$. Additionally, within R_1 , the ratio ℓ_{\parallel}/λ continues to rise, albeit at a reduced rate compared to the $100 - 600d_i$ range, where $\ell_{\parallel} \propto \lambda^{0.72 \pm 0.04}$. This slower rate of increase within R_1 can be attributed to the steepening of $SF_5^2(\ell_{\parallel})$ at scales marginally larger than R_1 .

As we move below the R_1 range and into the transition region (Sahraoui et al. 2009; Bowen et al. 2020a), the previously observed trend of increasing anisotropy ceases. Within the scale range of $2d_i \lesssim \lambda \lesssim 8d_i$, the eddies start to demonstrate more isotropic characteristics. This tendency towards isotropy peaks at $\lambda = 2d_i$, where the aspect ratio reaches $\lambda : \xi : \ell_{\parallel} = 1.56 : 1 : 1$. Throughout this scale range, the anisotropic scaling relations—derived from fitting curves to individual intervals and estimating the median values, presented along with the standard deviation of the mean—conform to $\ell_{\parallel} \propto \lambda^{2.01 \pm 0.06}$ and $\xi \propto \lambda^{1.25 \pm 0.05}$.

At even smaller scales, distinct scaling anisotropies characterize two separate ranges. Within $1d_i \lesssim \lambda \lesssim 2d_i$, the ratio ℓ_{\parallel}/λ shows an upward trend, following $\ell_{\parallel} \propto \lambda^{0.67 \pm 0.02}$, while the ratio ξ/λ remains relatively stable, adhering to $\xi \propto \lambda^{0.98 \pm 0.04}$. These findings stand in contrast to standard kinetic Alfvén wave (KAW) turbulence models (Howes et al. 2008; Schekochihin et al. 2009b) and deviate statistically from in-situ observations reported in (Duan et al. 2021; Zhang et al. 2022). However, they are in agreement with the intermittent

KAW model proposed by (Boldyrev & Perez 2012) and align with numerical kinetic simulations by (Cerri et al. 2019), as well as in-situ observations in the magnetosheath (Wang et al. 2020). At yet smaller scales, $0.5d_i \leq \lambda \leq 1d_i$, both ℓ_{\parallel}/λ and ξ/λ ratios exhibit an increase, scaling as $\ell_{\parallel} \propto \lambda^{0.5 \pm 0.05}$ and $\xi \propto \lambda^{0.87 \pm 0.04}$, respectively.

Figure 4 presents a three-dimensional representation of turbulence eddies, illustrating isosurfaces of SF_5^2 at various scales. This visualization was achieved by estimating conditional $SF_5^2(\ell, \theta_B, \phi_{\delta B_{\perp}})$, according to Equation 22, and utilizing 5° angular bins. The spherical polar coordinates $(\ell, \theta_B, \phi_{\delta B_{\perp}})$ obtained from this process were then converted into Cartesian coordinates $(\ell_{\parallel}, \xi, \lambda)$. Surfaces computed for the first octant were mirrored across to the other octants, based on the assumption of reflectional symmetry (Chen et al. 2012). In the 3D visualization, surface colors represent the distance from the origin, with cooler colors indicating larger distances. When these surfaces are projected onto different planes, the color denotes the distance from the origin of each respective plane. It is important to note that the colormap applied to these planar projections differs from the one used for the 3D representation. The color coding in these projections reflects the range of maximum and minimum distances observed across all three components.

5.3. Higher order statistics & Intermittency

We computed five-point structure functions, SF_5^n , for parallel, perpendicular, and displacement components, as per Equations 23 to 25, considering orders $n = 1, \dots, 10$ with $\omega = 10$. Additionally, we evaluated \mathbf{B} -trace structure functions, S_5^n . Furthering our analysis, we derived the normalized weighted average, SF_5^n ,

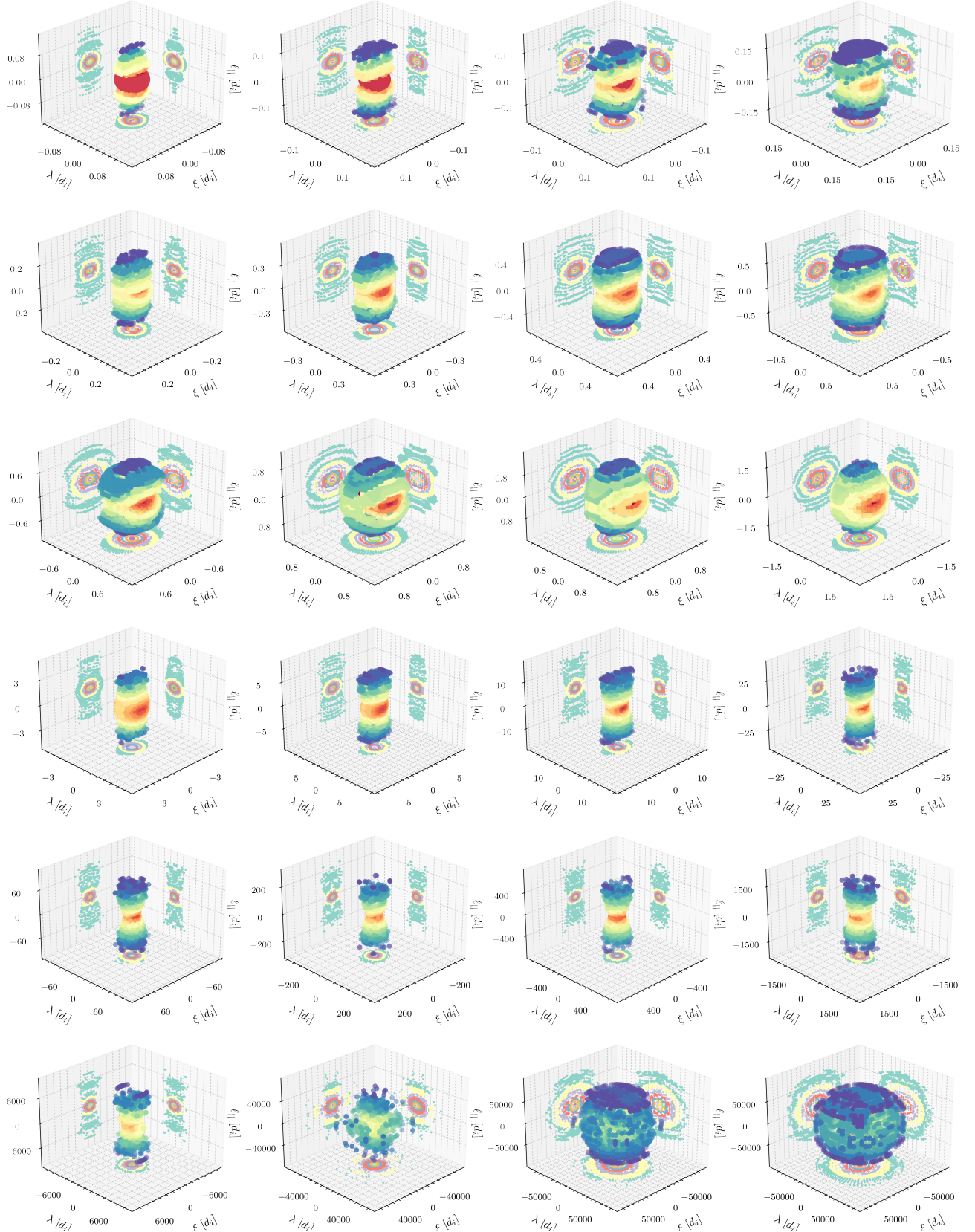


Figure 4. 3D representation of turbulence eddies obtained by estimating isosurfaces of constant energy of SF_5^2 at different levels, ranging from small scales (top left) to large scales (bottom right). The color scheme, although redundant, indicates the distance from the origin (0,0,0). Additionally, projections of the object onto each respective plane are displayed. While the projections share a common colormap to denote the distance from each plane's origin, the colormap for the 3D object differs.

for our dataset following Equation 26. After identifying two distinct sub-inertial ranges displaying clear power-law behavior, we calculated two sets of normalized structure functions. Within the R_1 domain, we normalized SF_5^n using $S_5^n(\lambda_*)$, where $\lambda_* = 50d_i$.

For the R_2 domain, normalization employed a different scale, $\lambda_* = 2 \times 10^3 d_i$. The latter normalized structure functions, particularly for the parallel, perpendicular, and displacement components, are depicted in Figure 5 panels (a) to (c), respectively. To aid visualization, each n -th order moment was vertically offset by 10^{-n} . Fitting each component of $\tilde{S}F_5^n(\ell)$ to a power law, $\propto \ell^{\zeta_n}$, facilitated the estimation of scaling exponents, ζ_n . The resulting ζ_n are depicted by red asterisks for the R_1 domain and gray for R_2 within the insets of the corresponding figure panels. For comparison, scaling exponent predictions based on the theoretical models proposed by CSM15 and MS17 are also included.

In the R_2 range, the scaling exponent ζ_n^λ of the perpendicular component forms a convex function of n , indicative of multifractal statistics and strong intermittency. This scaling profile closely aligns with the theoretical predictions by CSM15 and MS17, showing notable correspondence to the latter model at lower n values. For $SF_5^n(\xi)$, the observed scaling exponents, ζ_n^ξ , slightly deviate towards shallower gradients compared to the MS17 model. The scaling exponents of the parallel component $\zeta_n^{\ell_{\parallel}}$ exhibit a nonlinear dependence on n , though with less pronounced concavity than the perpendicular components, and notably diverge from the MS17 model, even at lower n values. A comprehensive discussion of these findings and their broader implications is provided in Section 6.

In the small-scale sub-inertial range, R_1 , the scaling exponents for both the parallel and displacement components display a linear relationship with n . Conversely, the scaling exponent ζ_n^λ of the perpendicular component forms a convex function of n , albeit demonstrating a lesser extent of non-linearity relative to that observed in the R_2 range. Overall, R_1 is characterized by less pronounced intermittency signatures compared to R_2 , with the observed ζ_n profiles deviating from the expectations set by established theoretical models.

To further investigate multifractality and deviations from Gaussian statistics in the magnetic field time series, we consider the Scale-Dependent Kurtosis, defined as $K(\ell) = SF^4(\ell)/[SF^2(\ell)]^2$ (Frisch 1995; Bruno et al. 2003). As a normalized fourth-order moment, $K(\ell)$ is sensitive to extreme values of increments, allowing us to detect the tendency of PDFs in intermittency-affected time series to exhibit increasingly flared-out tails at smaller scales. In simpler terms, it quantifies how the

“tailedness” of the distribution of increments in a turbulent field changes across various scales.

We employ both 2-point ($K_2(\ell)$) and 5-point ($K_5(\ell)$) methods to study the fractal properties of magnetic field time series. The resulting curves for the parallel, perpendicular, and displacement components of the magnetic field are illustrated in panels (a) to (c) of Figure 6. At scales $\lambda \geq 100d_i$, an increase in $K(\ell)$ is observed for all components towards smaller scales, indicating a progressive deviation from Gaussianity in the underlying PDFs of increments, a hallmark of multifractal statistics (Sorriso-Valvo et al. 1999).

The limitations of the 2-point method are particularly evident in the R_1 range, where it notably diverges from the 5-point approach. In the case of the perpendicular component, $K_2(\lambda)$ appears to plateau at $\lambda < 20d_i$, consistent with the findings of Chhiber et al. (2021). Conversely, $K_5(\ell)$ maintains an increasing trend in R_1 , albeit with a less steep slope compared to R_2 . Within the R_1 range, both the parallel, $K_5(\ell_{\parallel})$, and displacement, $K_5(\xi)$, components exhibit super-Gaussian but monofractal behavior, consistent with the linear $\zeta_n^{\ell_{\parallel}}$ and ζ_n^ξ profiles illustrated in Figure 5.

At kinetic scales, both $K_5(\lambda)$ and $K_5(\xi)$ exhibit an increasing trend towards smaller scales, while the behavior of the parallel component remains less distinct. This trend in the perpendicular component diverges from the monofractal statistics observed at sub-ion scales in several observational studies using K_2 (Wu et al. 2013; Chen et al. 2014; Chhiber et al. 2020). However, our findings align with hybrid and fully kinetic simulations by Cerri et al. (2019), where $K_5(\lambda)$ is demonstrated to increase above Gaussian values throughout the sub-ion scale range. Furthermore, qualitatively consistent trends were identified by Alexandrova et al. (2008), who utilized wavelet-derived kurtosis to observe a gradual increase in this measure at kinetic scales.

5.4. Scale-Dependent Dynamic Alignment & Critical Balance

We begin by examining the scale-dependent behavior of the alignment angle between the perpendicular components of the increments, $\delta\mathbf{b}_{\perp} - \delta\mathbf{u}_{\perp}$ and $\delta\mathbf{z}_{\perp}^+ - \delta\mathbf{z}_{\perp}^-$. Elsässer variable increments were determined as $\delta\mathbf{z}_{\perp}^{\pm} = \delta\mathbf{v}_{\perp} \pm \text{sign}(B_r^0)\delta\mathbf{b}_{\perp}$, where B_r^0 represents the 30-minute rolling average of the radial magnetic field component, B_r , used to determine the polarity of the background magnetic field. Here, \mathbf{z}_{\perp}^- and \mathbf{z}_{\perp}^+ denote inward and outward propagating Alfvén waves, respectively. Magnetic field data were downsampled, following the application of a low-pass Butterworth (1930) filter to mitigate aliasing, to match the temporal resolution of the ion moment

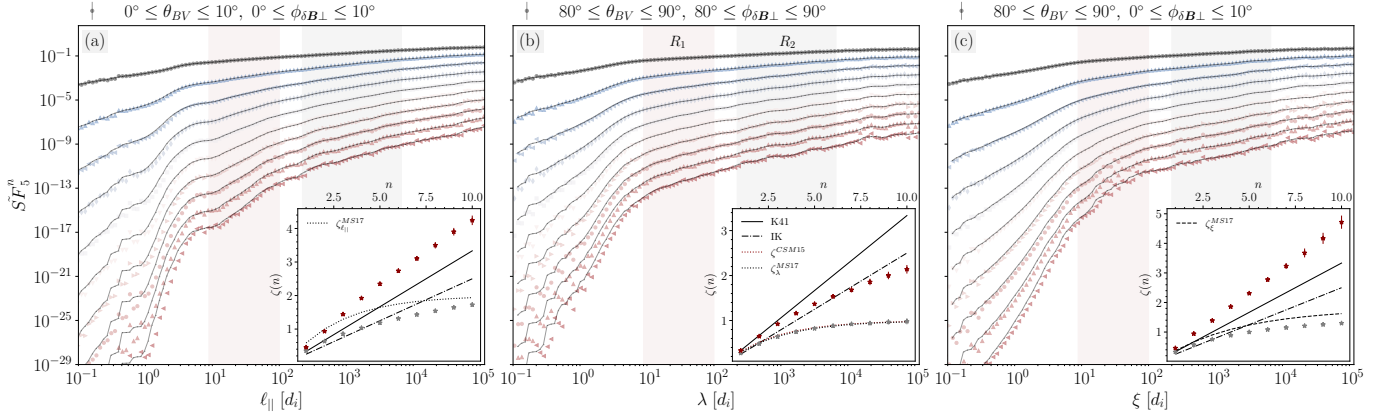


Figure 5. The main panels depict the normalized weighted average structure functions, $\tilde{S}F_5^n(\ell)$, for (a) parallel, (b) perpendicular, and (c) displacement components, each adjusted with a vertical offset for enhanced clarity. Prior to the weighted average estimation, each $SF_5^n(\ell)$ was normalized using the value of the trace $S_5^n(\lambda^*)$, where $\lambda^* = 2 \times 10^3 d_i$. These normalized averages, $\tilde{S}F_5^n(\ell)$, displayed in the main figure, were used to estimate ζ_n for R_2 , marked as gray asterisks in the insets. For ζ_n estimation in R_1 , indicated by red asterisks in the insets, a similar normalization process was applied at $\lambda^* = 50 d_i$. It is important to note that the latter normalized $\tilde{S}F_5^n(\ell)$ for R_1 are not depicted in the figure. Error bars in the insets represent the uncertainty associated with the power-law fits. For comparison, the scaling behaviors as predicted by the K41, IK, CSM15, and MS17 models are also included.

data. Magnetic field data were then normalized to velocity units using a 1-minute moving average applied to the proton density, n_p , time series.

Figure 7a,b illustrates two sets of alignment angles: $\theta_{\perp}^{ub(z)}$ in black, as defined by Equation 10, and $\tilde{\theta}_{\perp}^{ub(z)}$ in blue, calculated according to Equation 13. These sets are referred to as Θ^z when discussing Elsässer variables and Θ^{ub} in the context of velocity-magnetic field fluctuations, with the angle range confined to $0^\circ - 90^\circ$, consistent with Podesta et al. (2009). The inset of Figure 7b illustrates the normalized residual energy, σ_r , in red, and the normalized cross helicity, σ_c , in gray.

At the energy injection range, $\lambda \gtrsim 2 \times 10^4 d_i$, a trend towards tighter alignment at smaller scales is observed, predominantly in Θ^{ub} . This is accompanied by a monotonic increase in σ_c and a shift of σ_r towards more negative values. These trends are more pronounced over longer observational intervals, although such extended periods are beyond the scope of this analysis.

Within the R_2 range, θ^z exhibits negligible variation with scale. Conversely, $\tilde{\theta}^z$ reveals subtle signatures of enhanced alignment at $\lambda \lesssim 2 \times 10^3 d_i$, coinciding with σ_r transitioning from negative to positive values. Simultaneously, Θ^{ub} steadily increases, indicating progressive misalignment between the magnetic field and velocity increments at inertial scales.

The disparity between the two alignment definitions becomes more evident in the R_1 range, where $\tilde{\theta}^z \propto \lambda^{0.11}$. However, observations concerning this range should be approached cautiously due to potential instrumental noise, a matter further explored in Section 6.

What appears to solidly be the case, however, is that an inverse relationship holds between the alignment angle and the intensity of the field gradients. This relationship is depicted in the inset panel of Figure 7a, where θ^{ub} is plotted across various scale-dependent percentile bins of the Partial Variance of Increments (PVI) diagnostic, $\mathcal{I}_{\mathbf{B}}(t, \ell) = |\delta \mathbf{B}(t, \ell)| / \sigma_{\mathbf{B}}$, with $\sigma_{\mathbf{B}}$ representing the standard deviation calculated over a moving window of 1 hour, (Greco et al. 2018). Specifically, at $\lambda \gtrsim 2 \times 10^2 d_i$, higher-percentile $P(\mathcal{I}_{\mathbf{B}})$ bins are characterized by lower average θ_{\perp}^{ub} values. Similar results were obtained when considering θ_{\perp}^z and segregating alignment angles based on the percentile bins of the PVI diagnostic applied to the \mathbf{z}_{\perp}^{\pm} time-series, $\mathcal{I}_{\mathbf{z}^{\pm}}$.

Under the assumption that the cascade is local in λ , we investigated the scale-dependence of the nonlinearity parameter χ^{\pm} , according to the formulations by B06 and CSM15: $\chi^{\pm} = (\ell_{\parallel, \lambda}^{\pm} / \lambda^{\pm}) / (\delta z_{\lambda}^{\mp} / V_a) \sin \theta^z$. The analysis of outgoing (χ^+) and ingoing (χ^-) waves, depicted in gray and red respectively in panel (c) of Figure 7, reveals that both cascades start weak, with $\chi^{\pm} < 1$. As the cascade progresses towards smaller scales, a significant increase in the wave to nonlinear times ratio leads to a consistent rise in χ^{\pm} , continuing until scales nearing the R_2 range onset.

For the ingoing waves, a transition from weak to strong wave turbulence is noted, with $\chi^- > 1$ at $\lambda \approx 3 \times 10^4 d_i$. The cascade remains strong throughout the resolvable portion of the inertial range, with χ^- being scale-independent, staying close to, yet slightly greater than, 1.

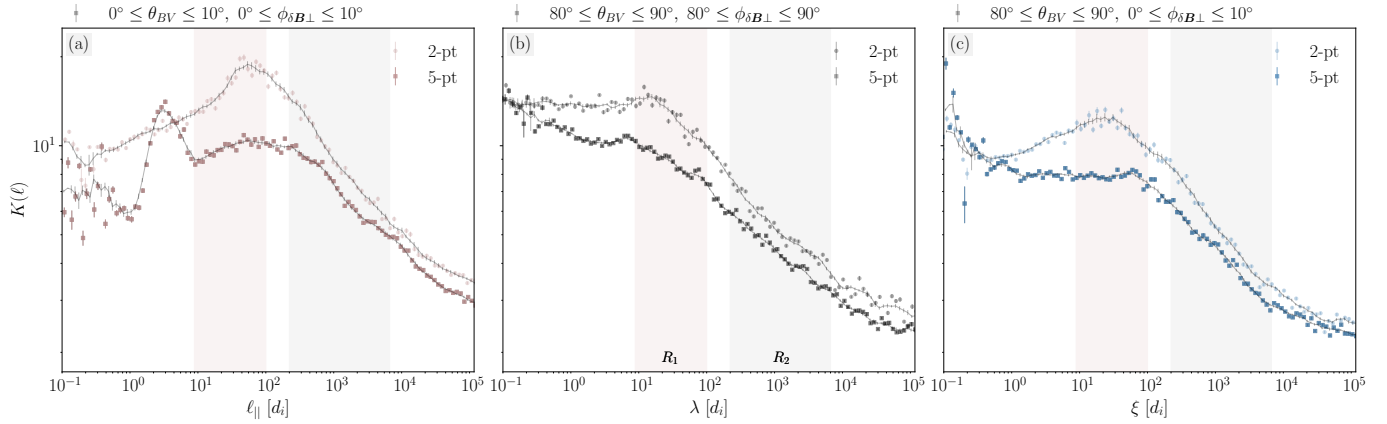


Figure 6. The scale-dependent kurtosis of the magnetic field, denoted as K_5 and K_2 , is estimated using 5-point structure functions (SF_5^n) and 2-point structure functions (SF_2^n), respectively. These are plotted in red, gray and light-blue, respectively, as a function of scale in units of ion inertial length (d_i) for the parallel (a), perpendicular (b), and displacement (c) directions. Power-law fits have been applied to K_5 over the region R_2 .

In contrast, the cascade of outwardly propagating waves remains weak within the R_2 range. More specifically, χ^+ shows a modest increase from approximately 0.1 at $\lambda = 10^4 d_i$ to around 0.2 at $\lambda = 2 \times 10^2 d_i$.

The potential inaccuracies in velocity measurements, exacerbated at smaller scales, along with the limited resolution of velocity field data, caution against drawing definitive conclusions about the cascades' nature in the R_1 range.

Lastly, it's noteworthy that the definition of χ^\pm , as proposed by GS95, was also considered. This analysis revealed a scale dependence similar to that of χ^\pm , but with both χ^\pm values being approximately twice as high.

6. DISCUSSION

Recent in-situ observations indicate that the regime canonically identified as the inertial range comprises two sub-inertial segments, exhibiting distinct scaling behaviors (Wicks et al. 2011; Chhiber et al. 2021; Sioulas et al. 2022; Telloni 2022; Wu et al. 2022; Sioulas et al. 2023; Sorriso-Valvo et al. 2023).

Building on this insight, our study investigates the anisotropic properties and higher-order statistics of the two sub-inertial ranges, utilizing a physically motivated, locally defined coordinate system. Concurrently, we focus on evaluating the predictions of homogeneous MHD turbulence models, grounded in the principles of *critical balance* and *dynamic alignment*, as proposed by CSM15 and MS17.

In the ensuing section, we embark on a detailed comparison with previous theoretical, observational, and numerical results that contextualizes our findings.

6.1. Investigating the Impact of Imbalance and Expansion on the Higher-Order Statistics

Phenomenological treatment of homogeneous MHD turbulence (e.g., GS95, B06, CSM15, MS17) is usually performed under the simplifying assumption of negligible cross helicity. However, the statistical properties of solar wind turbulence vary significantly with the degree of Elsässer and Alfvénic imbalance (Podesta & Borovsky 2010; Chen et al. 2013; Wicks et al. 2011; Wicks et al. 2013b; Bowen et al. 2018; Andrés et al. 2019; Sorriso-Valvo et al. 2021; Sioulas et al. 2023; D'Amicis et al. 2022; McIntyre et al. 2023). Various models have been proposed as modifications to the frameworks of GS95 and B06, incorporating different assumptions about the turbulent cascade to address the imbalance in oppositely directed Alfvénic fluxes (Lithwick et al. 2007; Beresnyak & Lazarian 2008; Chandran 2008; Perez & Boldyrev 2009; Podesta & Bhattacharjee 2010; Schekochihin 2022). As these models omit considerations of intermittency, they will not be elaborated upon in the ensuing discussion.

From an observational standpoint, the extent to which imbalance impacts higher-order statistics in MHD turbulence, is largely unexplored territory. Previous investigations have predominantly focused on categorizing findings based on wind speed or analyzing mixed Fast/Slow streams (Horbury & Balogh 1997b; Mangeney 2001; Salem et al. 2009; Chhiber et al. 2021; Wu et al. 2023), with a recent shift in interest towards magnetic compressibility (Palacios et al. 2022). However, these studies often do not explicitly detail the degree of Elsässer imbalance in the dataset, making direct comparisons with our observations challenging. Nonetheless, it is worth pointing out that the scaling profiles observed in the R_2 range, especially for the parallel and perpendicular components, qualitatively align with results presented in Osman et al. (2012).

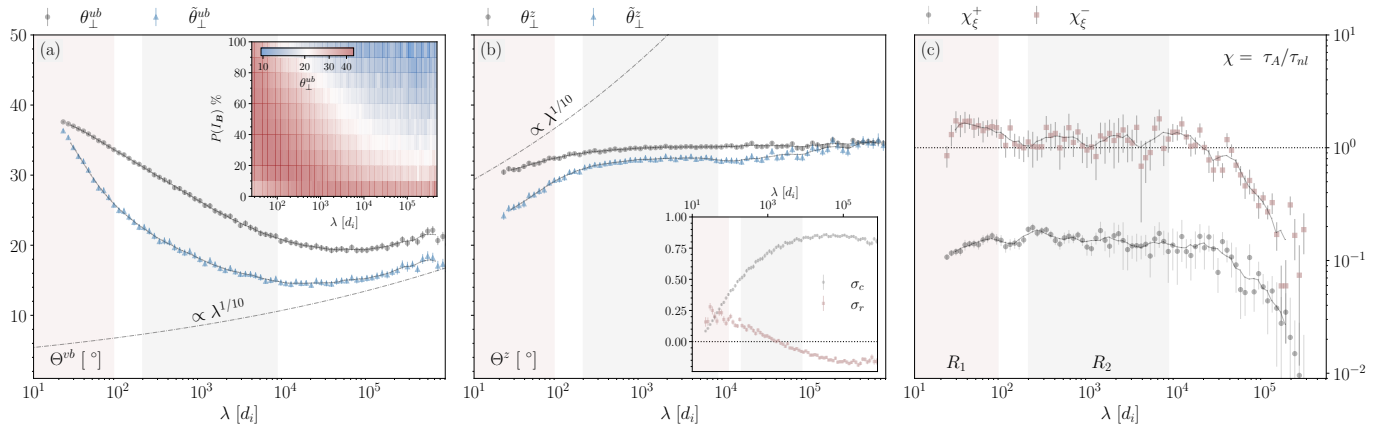


Figure 7. Alignment angles (a) $\Theta^{ub}(\lambda)$ and (b) $\Theta^z(\lambda)$, constrained to the range of $0^\circ \leq \Theta^{ub(z)} \leq 90^\circ$. The black curves depict alignment angles calculated with Equation 10, whereas the blue curves are based on Equation 13. The inset in panel (a) highlights the inverse relationship between alignment angle and field gradients by color-coding θ^{ub} across scale-dependent percentile bins of I_B . The i -th bin at scale λ is defined as $[10(i-1), 10i]$, for $i = 1, \dots, 10$. The inset in panel (b) displays $\sigma_r(\lambda)$, in red, and $\sigma_c(\lambda)$, in gray. Panel (c) shows the nonlinearity parameter, $\chi^\pm(\lambda)$, for outwardly (δz^+) and inwardly (δz^-) propagating waves, depicted with gray and red lines respectively. For all cases, results were derived by first calculating values for each interval independently and then computing a scale-dependent median.

In terms of numerical simulations, both homogeneous and inhomogeneous setups have been employed to examine the influence of imbalance on MHD turbulence statistics. Studies have primarily concentrated on spectral properties, revealing inertial range scalings of $\alpha_\lambda = -3/2$ (Perez et al. 2012; Chandran & Perez 2019; Grappin et al. 2022; Meyrand et al. 2023).

Shi et al. (2023) investigated the effects of Elsässer imbalance on higher-order statistics using both homogeneous and EBM simulations, each initialized with varying degrees of imbalance. It was shown that EBM simulations initialized with $|\sigma_c| \approx 1$ result in higher-order moment scaling exponents consistent with the predictions of the CSM15 model. Conversely, simulations with lower values of σ_c exhibited scaling exponents showing a linear dependence on order n . The study also highlighted significant differences in higher-order scaling exponents between homogeneous and EBM simulations, even when initialized with identical levels of imbalance. For example, scaling exponents in homogeneous runs with $\sigma_c \approx 0$ were found to be convex functions of order and closely resembled the CSM15 model, in line with previous investigations (Chandran et al. 2015; Mallet et al. 2015; Palacios et al. 2022). Additionally, Shi et al. (2023) noted that in EBM simulations, the scaling properties displayed variations when higher-order moments were calculated from increments sampled in directions other than radial.

The latter observation is consistent with the findings of Verdini & Grappin (2015), who conducted a comparative analysis of balanced homogeneous and EBM simulations. They observed that while the homogeneous simu-

lations displayed three-dimensional anisotropy, in agreement with B06—a finding further corroborated by Mallet et al. (2016)—the EBM simulations demonstrated axisymmetry relative to \mathbf{B}_ℓ and did not exhibit three distinct inertial range scaling laws. Specifically, EBM simulations with increments measured along the radial direction demonstrated spectral scalings of $\alpha_\lambda \approx \alpha_\xi \approx -3/2$ in both the perpendicular and displacement components. However, measurements in the transverse direction revealed scalings of $\alpha_\lambda \approx \alpha_\xi \approx -5/3$. In both cases, the parallel component lacked convincing scaling properties, although it exhibited a slightly steeper spectrum compared to the perpendicular components.

These findings lead to the following interpretation: The large-scale flow, being radial rather than uniform, cannot be negated by a Galilean transformation. Consequently, the expansion introduces an additional axis of symmetry and fosters a scale-dependent competition between the mean-field and radial axes (Völk & Aplers 1973). Intuitively the effects of the expansion should be important when the non-linear time, τ_{nl} is slower than the expansion of the solar wind, $\tau_{exp} = R/V_{SW}$, $\tau_{exp} \leq \tau_{nl}$. Given that τ_{nl} is scale-dependent, it logically follows that the effects of expansion are more pronounced at larger scales⁷. From this discussion, it becomes evident that the expansion has the potential to modify the local 3D anisotropy in a scale-dependent manner.

⁷ Note, however, that observational evidence suggests that expansion can contaminate the turbulence statistics even within inertial scales (Verdini et al. 2018, 2019)

At the resolution currently achievable in (R)MHD simulations, meaningful comparisons are possible with the larger-scale end of the inertial range, R_2 , spanning $200 - 6000d_i$. Focusing on ζ_λ and setting aside anisotropy, our findings are consistent with Shi et al. (2023)’s imbalanced EBM results and, consequently, with the models of CSM15 and MS17. Nevertheless, the observed discrepancies in the scaling exponents of the parallel and displacement components within R_2 could hint at the influence of expansion effects, suggesting a scenario where the dominant axis of symmetry is a mix of both B_ℓ and the radial axis, with the contribution of each being scale-dependent.

Shifting focus to the scaling exponents in R_1 (spanning $8 - 100d_i$), recent theoretical work suggests that under conditions of strong imbalance, generalized helicity conservation may hinder turbulent energy transfer to kinetic scales (Passot et al. 2018; Passot & Sulem 2019; Meyrand et al. 2021; Passot et al. 2022). The ‘‘helicity barrier’’ effect could influence both spectral and potentially higher-order moment scalings at the smaller end of the inertial range. Homogeneous hybrid-kinetic simulations, initialized under strong imbalance conditions to capture this effect (Squire et al. 2022a), exhibit spectral exponents for the parallel and perpendicular magnetic field components, $a_{\ell_\parallel} \approx -2$ and $a_\lambda \approx -5/3$ respectively, in line with observations in the R_1 range.

While our current data does not definitively link our observations to the helicity barrier effect, it underscores the necessity for more comprehensive numerical studies focusing on the higher-order statistics of strongly imbalanced turbulence.

In conclusion, this discussion underscores the significant impact of imbalance and expansion effects on MHD turbulence statistics, indicating that the solar wind might not provide an ideal laboratory for evaluating homogeneous MHD turbulence models. This realization calls for a prudent application of homogeneous, balanced turbulence models in the analysis of solar wind observations and highlights the imperative for more sophisticated theoretical modeling and refined data interpretation techniques.

6.2. Critical Balance (CB)

Using balanced RMHD simulations, Mallet et al. (2015) demonstrated that although the distributions of τ_{nl} and τ_A are not self-similar, their ratio, χ , maintains a scale-invariant distribution within the inertial range. Chhiber et al. (2020) employed balanced incompressible MHD simulations to show that while the χ distribution peaks at $\chi \approx 1$, it is asymmetric and skewed towards $\chi \geq 1$. Further reinforcing the Chhiber et al. (2020)

findings, Oughton & Matthaeus (2020) highlighted that, despite RMHD simulations producing results claimed to support CB, the similarity between RMHD’s $\chi \geq 1$ requirement and the CB condition of $\chi \approx 1$ has led to some confusion in differentiating these two theoretical frameworks.

Chen (2016) utilized an extensive dataset of fast wind streams with moderate cross-helicity ($\sigma_c \approx 0.6$) from the outer heliosphere to investigate the scale dependence of the non-linearity parameter. They found χ to be scale-independent across the inertial range, maintaining a value around $\chi \sim 1$. Due to the lower resolution in velocity data and a less pronounced imbalance compared to our dataset, they assumed identical statistical properties for the two Elsässer fields, enabling them to estimate $\chi = (\ell_\parallel/\lambda)(\delta b/V_A)$ using solely magnetic field data.

However, numerical simulations by Beresnyak & Lazarian (2008, 2009) suggest that with increasing imbalance, statistical properties (i.e., amplitudes, coherence lengths) of the two Elsässer species diverge progressively. Considering the strong imbalance in our dataset, we employed a more refined approach, computing $\chi^\pm = (\ell_{\parallel,\lambda}^\pm/\lambda^\pm)/(\delta z_\lambda^\mp/V_a)\sin\theta^z$.

Our analysis reveals a strong cascade for the inwardly propagating waves, with χ^- remaining scale-independent across the inertial range, maintaining a value slightly above unity. In contrast, the outwardly propagating waves exhibit a weaker cascade, with χ^+ increasing from 0.1 at $\lambda \approx 10^4d_i$ to 0.2 at $\lambda \approx 10^2d_i$.

At this point, it’s important to recognize two key factors that might affect the accuracy of our χ^\pm estimates. First, there’s a prevailing assumption that z^\pm structures are primarily sheared by counter-propagating z^\mp wavepackets of similar perpendicular scale, which implies a cascade that is local in λ . However, this notion is challenged by the work of Schekochihin (2022) who put forward a model of imbalanced turbulence that consists of two strong, ‘‘semi-local’’ cascades: one local in λ for the stronger field and another, local in ℓ_\parallel , for the weaker field. The implications of this model cast doubt on our estimates of χ^\pm that is predicated on the concept of scale locality.

Furthermore, the transition from weak to strong turbulence, characterized by a change from $\chi \ll 1$ and $\alpha_\lambda \approx -2$ to $\chi \approx 1$ and $\alpha_\lambda \approx -3/2$, is a pivotal aspect of the CB discussion. This transition, observed in balanced RMHD shell-model simulations Verdini & Grappin (2012), 3D incompressible MHD simulations (Meyrand et al. 2016), and recently in the Earth’s mag-

netosheath (Zhao et al. 2023), remains unreported in the solar wind ⁸.

Our results indicate a transition in the cascade of the ingoing wave from weak to strong turbulence, with $\chi^- > 1$ at $\lambda \approx 3 \times 10^4 d_i$, yet without capturing the anticipated scaling transition. We speculate, below, that this could be related to the effects of “anomalous coherence”. More specifically, in the context of homogeneous MHD, nonlinear interactions between counterpropagating waves are uncorrelated and transient, limited to the duration of encounters. In the solar wind, however, nonlinear dynamics are complicated by *anomalous coherence*, a phenomenon arising from non-WKB reflection of outwardly propagating fluctuations (Velli et al. 1989; Velli et al. 1990; Hollweg & Isenberg 2007). A key aspect of this effect is the presence of an “anomalous” reflected component, z_a^- , in addition to the “classical” component z_c^- , which remains stationary relative to the z^+ frame, coherently shearing it throughout its lifetime (Verdini et al. 2009; Chandran & Perez 2019). Under strong imbalance and inhomogeneity, z_a^- can assume a leading role at large scales, altering the phenomenology of the energy cascade and leading to distinct spectral behaviors: a $1/f$ scaling for outwardly propagating waves and an $f^{-3/2}$ scaling for inwardly propagating waves (Velli et al. 1989; Perez & Chandran 2013; Meyrand et al. 2023).

In summary, our results suggest that at inertial scales, outgoing waves experience a weak cascade, while ingoing waves undergo a strong one, closely resembling the CB condition ($\chi_\xi^- \approx 1$). However, given the complexities previously discussed and the uncertainties inherent in our measurements, we advise interpreting these findings with a degree of caution.

6.3. Scale Dependent Dynamic Alignment (SDDA)

Several numerical investigations into homogeneous (R)MHD (Mason et al. 2006; Perez et al. 2012, 2014; Cerri et al. 2022) have provided ample evidence for alignment signatures spanning a significant portion of the inertial range. However, Beresnyak (2012, 2014) have suggested that this observed alignment increase may be a finite-range phenomenon closely linked to dynamics at the outer scale.

Observational studies using data sampled at 1 AU have provided evidence of alignment at large, energy-containing scales. However, it has been observed that this trend towards increasing alignment diminishes at inertial scales (Podesta 2009; Hnat et al. 2011; Wicks

et al. 2013a; Parashar et al. 2019). This trend persists even in data intervals specifically chosen to mitigate the effects of solar wind expansion (Verdini et al. 2018). It has been noted, however, that small errors in velocity vector measurements, due to instrumental limitations, can lead to significant errors in alignment angle measurements, even at large scales (Podesta et al. 2009).

Recently, Parashar et al. (2020) explored the scale dependence of several alfvénicity diagnostics during E1 of PSP. Their findings suggest that σ_c starts decreasing, with σ_r increasing, at scales considerably larger than those observed at 1 AU (Podesta & Borovsky 2010), despite high alfvénicity at large scales. This observation aligns with HELIOS observations (Tu et al. 1990) and has been attributed to the substantial energy found in velocity shears in the inner heliosphere (Ruffolo et al. 2020). Specifically, shear disrupts an initial spectrum of high cross helicity by injecting equal amounts of the two Elsässer energies (Roberts et al. 1987; Goldstein et al. 1989; Roberts et al. 1992).

The scale-dependence of the alignment angles correlates directly with that of σ_c and σ_r , as only two out of these four quantities are independent. Specifically, the formal relationship between imbalance, residual energy, and alignment, as described by $\cos\theta_\perp^z = \sigma_r/(1 - \sigma_c^2)^{1/2}$ and $\cos\theta_\perp^{ub} = \sigma_c/(1 - \sigma_r^2)^{1/2}$, indicates that the development of both Elsässer imbalance and residual energy, i.e., a monotonic increase in $|\sigma_c|$ and $|\sigma_r|$ towards smaller scales, is necessary for SDDA to emerge towards smaller scales (Wicks et al. 2013a; Schekochihin 2022).

Such trend is evident in Figure 7, where alignment signatures become apparent only when σ_c exhibits a monotonic increase at scales $\lambda < 10^4 d_i$, or when σ_r becomes positive, leading to a monotonic increase in $|\sigma_r|$ at scales $\lambda < 2 \times 10^3 d_i$. Although instrumental noise might influence the latter trend, as discussed in Bourouaine et al. (2020), the observed behavior at energy injection scales aligns with 1 AU observations (Wicks et al. 2013a). In contrast, in the inertial range, $\theta^z (\approx 35^\circ)$ remains roughly scale-independent.

These observations raise a critical question: Is the observed scale-dependence of the alignment a reflection of actual physical processes, or might it simply be a consequence of instrument characteristics?

Potential physical mechanisms may encompass interactions between compressive and non-compressive modes (Cho & Lazarian 2003; Chandran 2005), ideal MHD instabilities manifesting in the solar wind, including the Kelvin-Helmholtz instability (Malagoli et al. 1996), the cessation of the aligning cascade due to the tearing instability (Mallet & Schekochihin 2017; Boldyrev & Loureiro 2017; Comisso et al. 2018), or

⁸ Even though such a transition was speculated in recent works (Telloni 2022; Wu et al. 2022; Sioulas et al. 2023)

even the solar wind’s inherent inhomogeneity resulting in non-WKB reflections and a reduction in cross-helicity.

The extent to which instrumental noise influences these observations remains a crucial, yet unresolved, concern, emphasizing the necessity for a careful interpretation of observational data. While our analysis cannot definitively assert the nature of SDDA at small scales, it provides compelling observational evidence suggesting an inverse relationship between alignment angles and the intensity of field gradients, thereby corroborating the numerical results of Mallet et al. (2015). As such, our observations lend support to the CSM15 model, suggesting that the physical basis of alignment lies in the mutual shearing of Elsässer fields during imbalanced collisions between counterpropagating wave packets.

Before concluding, another topic related to our findings deserves further discussion. Our observations indicate strong anti-alignment between Elsässer species at larger scales, with $\sigma_c \approx 1$ and typically small and negative σ_r , implying, as suggested by Wicks et al. (2013a), $\cos\theta_{\perp}^z \approx 180^\circ$ at $\lambda \approx 10^4 d_i$. It is natural, then, to inquire how this picture would be modified in the case of globally balanced streams. For instance, as emphasized in CSM15, outer-scale fluctuations in the context of globally balanced turbulence are not expected to be strongly aligned. This suggests that while imbalanced turbulence may exhibit alignment saturation at larger scales, balanced turbulence has the potential for further alignment, assuming that σ_c has room to increase at smaller scales. Thus, the dynamics of alignment across scales in balanced turbulence present an intriguing area for future research, particularly in comparing the extent of this alignment process with that in imbalanced streams. This aspect warrants further investigation and will be the focus of future work.

6.4. Exploring the Efficacy of the CSM15 & MS17 Models in the Context of Imbalanced Turbulence

Our results indicate that the intermittent scalings of the n th-order conditional structure functions in the direction perpendicular to both the local mean field and the fluctuation directions closely align with the theoretical frameworks proposed by CSM15 and MS17. However, our dataset exhibits notable characteristics that diverge from the assumptions underlying these models. These include strong imbalance in the fluxes of the Elsässer species and a prevalence of eddies conforming to a field-aligned tube topology, which, on average, do not display increasing alignment towards smaller scales. At first glance, these observations might seem contradictory to the expectations set forth in the aforementioned models. Nevertheless, upon closer examination of the

model’s fundamental assumptions, it becomes apparent that these empirical findings are not inconsistent with the model’s theoretical framework.

In Section 2, we examine the foundational assumptions of the CSM15 and MS17 models. These assumptions encompass (1) negligible cross helicity at energy injection scales and (2) the formation of eddies following a current sheet topology, characterized by a volume filling factor $f_{cs} \propto \lambda$, alongside the dynamic alignment of vector field fluctuations at smaller scales. The models incorporate alignment as an intermittency effect, resulting in (1) the inherent introduction of local Elsässer imbalance and (2) the lack of a requirement for the “average” eddy to adhere to a 3D anisotropic current sheet topology. The models propose that it is the eddies in the tails of the PDFs that are expected to exhibit this topology, showing increased alignment at smaller scales. In essence, an inverse correlation between alignment and the intensity of field gradients is anticipated at any given scale.

When second-order moments are employed to examine the statistical shape of eddies, the high-amplitude, current-sheet-like structures found in the tails of the increment PDFs are typically obscured during the averaging process by more common, lower-amplitude, tube-like eddies. However, as higher moment orders are considered, these high-amplitude structures gain more prominence in the ensemble average, thereby significantly impacting the profile of the scaling exponents.

Given that fluctuations in the perpendicular component are energetically dominant, any “side effects” stemming from the disruption of anisotropy due to expansion, and possibly from constraints imposed by spherical polarization (Matteini et al. 2024), do not seem to significantly impact the scaling characteristics of the perpendicular component. However, they do appear to influence the scaling profiles of the displacement and parallel components. Hence, incorporating these effects into the existing homogeneous models could potentially enhance the scaling predictions of these models and offer valuable insights into the nature of intermittent turbulence in the expanding solar wind.

6.5. Observations of the outer scale

At large energy-containing scales, as depicted in Figure 3, the parallel and perpendicular components display rough equipartition in fluctuating energy. However, the displacement component appears somewhat more energetic in comparison. Consequently, eddies deviate from isotropy, exhibiting a subtle compression along the fluctuation direction.

Our findings contrast with those of [Chen et al. \(2012\)](#), who observed eddy elongation along the displacement direction ($\hat{\xi}$) at large scales in fast solar wind data at 1.4 AU.

To delve deeper into these findings, [Verdini & Grappin \(2015\)](#) conducted a comparative analysis using 3D MHD homogeneous and EBM simulations. They found isotropic eddies at energy injection scales in non-expanding simulations. However, in expanding simulations where increments were measured along the radial direction (typical for single-spacecraft missions at 1 AU), results aligned with those reported by [Chen et al. \(2012\)](#). Interestingly, large-scale anisotropy disappeared, and eddies appeared isotropic when increments were measured in non-radial directions. This was interpreted as an effect of expansion, which preferentially dampens the radial component of magnetic field fluctuations relative to the azimuthal ones, confining fluctuations primarily to the plane orthogonal to the radial direction and leading to an anisotropic energy distribution among the field components. This phenomenon was observed in 3D EBM simulations (see e.g., [Dong et al. 2014](#)).

In a more recent study, [Verdini et al. \(2018\)](#) analyzed a decade of data from the Wind spacecraft and identified a correlation between large-scale anisotropy and variance anisotropy, defined as $E = (b_T^2 + b_N^2)/b_R^2$, where b represents the rms amplitude of fluctuations. They found that intervals corresponding to the “strong” expansion dataset (defined by $E > 2$) exhibited eddy elongation along the displacement direction, consistent with [Chen et al. \(2012\)](#). Conversely, intervals from the “weak” expansion dataset (with $E \leq 2$) showed eddy elongation along the perpendicular direction ($\hat{\lambda}$).

Based on these results, [Verdini et al. \(2018\)](#) suggested that PSP, due to its unique orbit—allowing measurements perpendicular to the radial direction during its near-sun phase—would detect isotropic eddies at energy injection scales.

To overcome the limitations of single spacecraft measurements, [Vech & Chen \(2016\)](#) adopted a multispacecraft approach, enabling the separation of measurements along both radial and transverse directions. This strategy facilitated the isolation of expansion, solenoidality, and the mean magnetic field effects. Their investigation underscored the dominant role of the solenoidality constraint ([Turner et al. 2011](#)) over expansion in contributing to the observed variance anisotropy, E (see e.g., [Horbury & Balogh 2001](#)). They further noted that while some anisotropy, as observed with radial increments, stemmed from expansion, a reduced yet noticeable degree of anisotropy persisted when measurements

were conducted along the transverse direction. This suggests the involvement of additional mechanisms in shaping the large-scale 3D anisotropy.

Recent in-situ observations have shed light on the decay observed in the radial component within the inner heliosphere, indicating that it cannot be solely attributed to expansion effects. Specifically, analysis of data from PSP and HELIOS by [Tenerani et al. \(2021\)](#) demonstrated that the rms of fluctuations in the radial component decays at a slower rate compared to that of the perpendicular component. This phenomenon was further clarified by [Matteini et al. \(2024\)](#), who attributed it to the tendency of magnetic field fluctuations in the solar wind to evolve towards a state of spherical polarization. The spherical polarization imposes constraints on the radial component’s rms fluctuations, leading to a decay described, particularly at large scales, by $b_r \sim b/2B$ (see also, [Squire et al. 2020](#); [Mallet et al. 2021](#)).

Returning to our findings, we observe only a slight deviation from isotropy at the outer scale, which is notable considering that our dataset falls within the strong expansion category, with an average variance anisotropy of $E \approx 4.26 \pm 3.51$. Additionally, the sampling angle consistently falls within the range of $\theta_R \in [160^\circ, 180^\circ]$, indicating quasi-radial sampling. Despite identifying several intervals among multiple PSP encounters that exhibit isotropic large-scale eddies, no clear correlation has emerged from this preliminary analysis between prevailing plasma signatures (e.g., E , σ_c , σ_r , θ_R) and the occurrence of such intervals.

Taking into account the subtleties revealed by the recent observations discussed above, we must recognize our current inability to offer a satisfactory explanation for the observed configuration of the large-scale eddies in our dataset. However, the differences noted in the near-Earth and near-Sun eddies could indicate preferential damping in the fluctuations of the displacement component of the magnetic field. To clarify this aspect, it would be worthwhile to explore the development of the large-scale eddies at varying heliocentric distances.

6.6. Isotropization of eddies at small scales

Figure 4 illustrates that within the R_1 range, the eddies display increasing anisotropy, resembling ribbon-like structures towards smaller scales. However, the trend of increasing aspect ratio ceases at $\lambda \approx 2d_i$, at which point the eddies transition toward a quasi-isotropic state. In the following, we discuss two potential mechanisms that could explain these observations.

The observed transition towards isotropy at smaller scales is consistent with the idea that thin, long-lived

current sheets generated by the turbulent cascade can be disrupted by the tearing instability and subsequent reconnection (Furth et al. 1963). Specifically, when the maximum growth rate of the Coppi et al. (1976) mode, γ_t , representing the fastest tearing mode in an MHD sheet, becomes comparable to the non-linear cascade time τ_{nl} ($\gamma_t \tau_{nl} \gtrsim 1$), the stability of the current sheets is compromised (Pucci & Velli 2014; Uzdensky & Loureiro 2016). The instability leads to the fragmentation of the dynamically forming sheets into flux ropes, which exhibit isotropy in the plane perpendicular to the magnetic field. This phenomenon is expected to occur at scale, λ_D , beyond which the nature of the MHD cascade undergoes a significant transformation. The disruption of the current sheets affects the dynamic alignment, accelerating the turbulent cascade and resulting in a noticeable steepening of the power spectrum (Mallet et al. 2017; Loureiro & Boldyrev 2017; Boldyrev & Loureiro 2017).

While this mechanism appears feasible for balanced turbulence, as evidenced by observations in the solar wind (Vech et al. 2018) and more recent findings in 3D fully-compressible (Dong et al. 2022) and reduced (Cerri et al. 2022) MHD simulations, it’s important to acknowledge that the cutoff of the inertial range in imbalanced turbulence might also be influenced by kinetic effects. Therefore, despite the observation of a sub-ion-scale range mediated by magnetic reconnection in 2.5D hybrid-kinetic simulations (Cerri & Califano 2017; Franci et al. 2017), other kinetic-scale mechanisms in imbalanced turbulence could potentially contribute to eddy isotropization. For instance, an alternative explanation for the isotropization of the eddies at small scales could be associated with the recently discovered “Helicity Barrier” mechanism (Passot et al. 2018; Passot & Sulem 2019; Meyrand et al. 2021; Passot et al. 2022).

As discussed in the introduction, strongly magnetized (low-beta) collisionless plasmas exhibit nonlinear conservation of both energy and cross helicity. However, the conserved quantity in reality is termed “generalized helicity.” At $k_{\perp} \rho_i \lesssim 1$, this corresponds to the cross helicity following a forward cascade, which conservatively transforms into magnetic helicity at $k_{\perp} \rho_i \gtrsim 1$, undergoing an inverse cascade. Consequently, an imbalanced cascade arriving from the inertial range faces a complication—the sudden need to reverse the direction of the generalized helicity cascade. The helicity barrier impedes the viability of a constant-flux cascade, leading to an accumulation of energy in the stronger Elsässer field. This accumulation shortens τ_{nl} , reducing the parallel correlation length, in line with the CB theory, to the extent that turbulent energy is redirected into an (ICW;

(see, Stix 1992)) spectrum. This mechanism opens up a new dissipation channel via the ion-cyclotron resonance (Squire et al. 2022b).

ICWs are commonly observed in the nascent solar wind, particularly during intervals marked by (anti)alignment between the mean magnetic field and solar wind flow direction (Bowen et al. 2020b). A strong correlation exists between the presence of ion-scale waves and the level of imbalance of fluctuations at inertial scales (Zhao et al. 2022; Bowen et al. 2023). The presence of ICWs can significantly impact the power spectra of magnetic fields at ion kinetic scales (Bowen et al. 2020b; Shankarappa et al. 2023). Specifically, the bump observed in the parallel spectrum just before the transition region has been attributed to the presence of ICWs, suggesting that the isotropization of the eddies could be a consequence of the helicity barrier mechanism.

The main emphasis of this analysis is on the inertial and energy injection scales. The extended interval size allows for more reliable estimates of second-order moments and, consequently, the anisotropic curves presented in Figure 3. However, no effort has been made to account for the energy contribution ICWs. Due to the strong correlation between the presence of ion-scale waves and Elsässer imbalance, simply disregarding intervals with ICW wave signatures (Duan et al. 2021; Zhang et al. 2022) may impede our investigation into kinetic-scale turbulence statistics in strongly imbalanced intervals. An alternative approach would entail identifying and eliminating the energy attributed to ICWs from the observed energy spectrum (see e.g., Shankarappa et al. 2023; Wang et al. 2023), and examining the resulting anisotropy based on the parallel and perpendicular spectra. This will be the focus of an upcoming study.

6.7. *Can the trace PSD be interpreted as the perpendicular PSD ?*

The theoretical models discussed in Section 1 provide scaling predictions for the parallel, perpendicular, and displacement components of fluctuating fields.

However, the angle between the solar wind flow and the magnetic field, as observed by spacecraft, can significantly influence whether fluctuations in measured quantities vary parallel or perpendicular to the magnetic field. Due to the Parker Spiral configuration (Parker & Tidman 1958), the baseline value of the angle between the solar wind flow and the magnetic field, denoted as Θ_{VB} , increases with heliocentric distance. Consequently, spacecraft measuring magnetic field fluctuations at 1 AU are more likely to detect fluctuations perpendicular to the mean magnetic field direction.

Considering the strongly anisotropic nature of the turbulent cascade, with the majority of power associated with perpendicular wavenumbers (Shebalin et al. 1983; Montgomery & Turner 1981; Horbury et al. 2008), observational studies have traditionally estimated the trace PSD and interpreted these measurements as representative of the perpendicular spectrum. However, as the PSP moves closer to the Sun, both the flow and the magnetic field become predominantly radial. Consequently, PSP often detects variations parallel -resulting in a deficit of measurements perpendicular- to the magnetic field. This can impact the statistical signatures of MHD turbulence, including intermittency (Sioulas et al. 2022), estimates of correlation lengths (Cuesta et al. 2022), etc. As shown in Figure 2, the deficit caused by the sample size of the perpendicular fluctuations due to quasi-parallel sampling can also result in strong deviations between the perpendicular and trace PSD. This effect becomes even more important at later PSP encounters, and thus caution should be exercised when trying to utilize the trace PSD to compare with perpendicular PSD predictions of theoretical models.

6.8. *Assessing 2-Point Structure Functions for Small-Scale Turbulence Analysis*

The departure from monofractal statistics, exemplified by the adoption of SF_5^n , underscores the inadequacy of the SF_2^n method for statistical analysis of MHD turbulence at smaller spatial scales. Specifically, the SF_2^n method lacks accuracy in capturing the scaling behavior at these scales, where steep scaling in the power spectra and higher-order moments are frequently seen. This deficiency can result in imprecise estimations of all associated intermittency metrics, leading to potentially erroneous interpretations of the nature of the turbulent cascade (see also 3D kinetic simulations by Cerri et al. 2019).

The prolonged duration of the intervals examined in this study, which may not be optimal for a concentrated analysis at kinetic scales, in conjunction with the limitations posed by the presence of ICWs as discussed in Section 5.2, underscores the need for further investigation. Future studies should consider employing either 5-point or wavelet-derived structure functions, with a specific emphasis on distinguishing between balanced and imbalanced turbulence streams (see, e.g., Bowen et al. 2023). This comprehensive exploration is essential for achieving a deeper and more precise comprehension of the fractal properties of MHD turbulence at kinetic scales.

6.9. *Limitations*

In addition to the limitations associated with velocity measurements discussed earlier, it is essential to ac-

knowledge further inherent limitations in the analysis presented in this study.

6.9.1. *Finite sample size effects*

The proper study of MHD turbulence hinges on the ability to sample plasma from a common solar source, typically a single solar wind stream, and gather a sufficiently large sample size for statistical analysis. Spectral properties alone are insufficient for assessing scale invariance and fractal properties; higher-order moments are necessary. While evaluating structure functions is generally straightforward, estimating scaling exponents presents pitfalls. The primary concern arises from increased sensitivity to rare and large events as the order, p , increases. This can lead to finite sample effects dominating the analysis, especially as emphasis shifts to the poorly sampled tails of the distribution with higher orders. Consequently, higher-order moments become susceptible to outliers, rendering estimates of scaling exponents increasingly unreliable (Dudok de Wit et al. 2013; Palacios et al. 2022). As a rule of thumb, it is generally deemed safe to compute structure functions up to a certain order, typically defined as $p_{\max} = \log N - 1$, where N represents the sample size (Dudok de Wit et al. 2013).

In our analysis, these challenges are further compounded by two factors. Firstly, we employ conditional analysis to estimate higher-order moments in three physically motivated directions, resulting in the exclusion of a significant portion of increments falling outside specified angle ranges. Secondly, we utilize 5-point structure functions, where the way increments are taken leads to a larger portion of the time series being discarded due to edge effects.

Moreover, PSP data introduces added complexity compared to 1AU measurements, as the distance from the Sun rapidly changes, causing large variations in the rms of fluctuations between intervals sampled at different heliocentric distances. Consequently, very long intervals cannot be utilized effectively.

Despite these limitations, the present analysis could be significantly improved by adopting the method described in Palacios et al. (2022), where a large sample of increments from non-contiguous solar wind streams with similar characteristics can be utilized to construct the PDFs needed to obtain higher-order moments. This approach will be the focus of future work.

6.9.2. *Scaling exponents of Elsässer fields.*

In this study, our primary focus has been on the higher-order moments derived from the magnetic field timeseries. However, it's crucial to recognize that the fundamental variables in MHD are the Elsässer

fields—rather than \mathbf{B} and \mathbf{V} —due to their conservatively cascading energies. Indeed, the scaling predictions provided by the CSM15 and MS17 models pertain to the scaling exponents of the Elsässer field increment moments. Therefore, a more direct comparison with these models would entail estimating the moments of increments in \mathbf{z}^\pm (see e.g., Palacios et al. 2022). However, adopting this approach would require downsampling the magnetic field timeseries to synchronize with the cadence of the velocity field data. This would lead to a notable reduction in sample size, and render the estimation of anisotropic higher-order moments unfeasible with our current dataset.

Nevertheless, as discussed in CSM15, the regions contributing dominantly to both types of structure functions are those where $\delta\mathbf{z}^\pm$ exhibits exceptional magnitudes. In these regions, one Elsässer fluctuation, e.g., $\delta\mathbf{z}^+$, typically dominates over the other, leading to $\delta\mathbf{b} \approx (1/2)\delta\mathbf{z}^+$. Therefore, given the significant imbalance in our dataset, the scaling exponents estimated for the magnetic field timeseries can provide a reasonable approximation for the scaling exponents of the dominant (outgoing) Elsässer field.

6.9.3. Switchbacks

The near-Sun solar wind environment is characterized by the prevalent occurrence of Switchbacks, a subset of predominantly Alfvénic fluctuations with amplitudes significant enough to cause the magnetic field to reverse its direction abruptly, resulting in a local field polarity reversal and a corresponding radial velocity jet (Matteini et al. 2014; Horbury et al. 2018; Bale et al. 2019).

The question arises as to what extent these sudden reversals impact our ability to accurately estimate the local magnetic field, and consequently, the scaling exponents of the parallel and displacement components.

While excluding switchbacks from the analysis could potentially address this concern, it’s noteworthy that the majority of our samples for the two perpendicular components originate from substantial kinks in the magnetic field time series, as these events lead to large Θ_{BV} angles. Therefore, no attempt has been made to further clarify this aspect. However, it is reassuring to note that the scaling exponent profiles obtained for a substantial dataset of imbalanced Wind observations at 1 AU, where significant kinks in the magnetic field time series typically diminish and switchbacks/switchback patches transition into microstreams (Horbury et al. 2023; Soni et al. 2024), are qualitatively consistent with those reported in the current analysis.

7. CONCLUSIONS AND SUMMARY

We analyzed in-situ observations from a highly Alfvénic stream captured during Parker Solar Probe’s first perihelion to assess the predictions of MHD turbulence models grounded on the principles of “Critical Balance” and “Scale-Dependent Dynamic Alignment”. Our objective was to assess the extent to which the conjectures made and predictions derived by these models align with in-situ solar wind observations and establish solid observational benchmarks for the testing and refinement of MHD turbulence phenomenologies.

The main findings of our study can be summarized as follows:

At the outer scale, $\lambda \gtrsim 2 \times 10^4 d_i$, we find:

(a1) Both (out)ingoing waves undergo a weak cascade, $\chi^\pm < 1$, that strengthens towards smaller scales. The trend is concurrent with tighter scale-dependent dynamic alignment (SDDA) of fluctuations, a monotonic increase in cross-helicity (σ_c), and a shift towards more negative residual energy (σ_r) values

(a2) The ingoing waves transition to a strong cascade ($\chi^- \gtrsim 1$) at $\lambda \approx 3 \times 10^4 d_i$; the associated spectral scalings deviate from the expected weak-to-strong turbulence transitions. We explore the possibility that “anomalous coherence” effects may account for this discrepancy in Section 6.

The domain canonically identified as the inertial range is comprised of two distinct sub-inertial segments that exhibit distinct turbulence statistics.

For the subinertial range spanning $200 - 6000 d_i$ and termed R_2 we find:

(b1) Spectral scaling indices for components parallel to the local mean field, fluctuation (displacement), and perpendicular directions assume values of $\alpha_{\ell_{\parallel}} = -1.66 \pm 0.05$, $\alpha_{\xi} = -1.56 \pm 0.08$, and $\alpha_{\lambda} = -1.49 \pm 0.03$, respectively.

(b2) The “average” eddy assumes a field-aligned tube topology.

(b3) The alignment angle Θ^{ub} between velocity and magnetic-field fluctuations monotonically increases towards smaller scales, while the alignment Θ^z between the Elsässer fields remains roughly scale independent ($\approx 35^\circ$). In both cases, an inverse relationship between alignment angles and the intensity of field gradients is observed, suggesting that the physical basis of alignment lies in the mutual shearing of Elsässer fields during imbalanced collisions between counterpropagating wave packets, as suggested in CSM15.

(b4) The cascade is strong for inwardly propagating waves ($\chi^- \gtrsim 1$) but weak for outwardly propagating ones, with χ^+ increasing from 0.1 to 0.2 as scales decrease from $\lambda \approx 10^4 d_i$ to $10^2 d_i$.

(b5) The scaling exponents of the structure functions perpendicular to both \mathbf{B}_ℓ and the fluctuation direction conform to the theoretical models of CSM15 and MS17. However, the scaling profile in the parallel and displacement components deviates from theoretical predictions, possibly due to contamination from expansion effects.

For the subinertial range spanning $10 - 100 d_i$ (termed R_1), we find:

(c1) The spectrum steepens, with spectral scaling indices for components parallel to the local mean field, fluctuation (displacement), and perpendicular directions assuming values of $\alpha_{\ell_{\parallel}} = -1.97 \pm 0.05$, $\alpha_{\xi} = -1.94 \pm 0.06$, and $\alpha_{\lambda} = -1.64 \pm 0.04$, respectively.

(c2) A shift from isotropy in the plane perpendicular to \mathbf{B}_ℓ becomes evident, indicating a shift in eddy structures from tube-like to ribbon-like, $\ell_{\parallel} \gg \xi \gg \lambda$. While signatures of increasing SDDA are observed, the result is potentially susceptible to errors in particle data measurements.

(c3) The scaling exponents of the parallel and displacement components are a linear function of order, while the perpendicular component exhibits a weakly non-linear scaling profile. An overall transition towards “monofractal” statistics and a weakening of intermittency, compared to R_2 , are evident.

(d) At $\lambda \approx 8 d_i$, the increase in aspect ratio ceases, and the eddies transition to a quasi-isotropic state. This shift might be a signature of the tearing instability, potentially leading to reconnection of the thin current sheets, or it could result from turbulent energy being channeled into an ion-cyclotron wave spectrum, consistent with the “helicity barrier” effect.

(e) The 2-point structure function method SF_2^n is inadequate for capturing the essential properties of the turbulent cascade, at smaller scales. To accurately characterize steeper power laws at smaller spatial scales, the use of a more sophisticated method such as the 5-point structure function SF_5^n is essential.

While our study doesn’t delve into the direct application of diagnostics for expansion and imbalance effects, it’s interesting to note that preliminary findings using data from the Wind mission show a notable correspon-

dence with the results from EBM simulations conducted by Shi et al. (2023). Specifically, the scaling exponents in R_2 are consistent with CSM15 when $\sigma_c \approx 1$, and become a linear function of order as the imbalance decreases to $\sigma_c \approx 0$. Furthermore, extending the work of Verdini et al. (2018) to higher order moments it is found that when intervals are selected in such a way as to minimize the expansion effects the scaling exponents in all three components are in striking agreement with those predicted by the MS17 model (Sioulas et al. 2024, in progress).

In summary, our findings suggest that the models proposed by CSM15 and MS17, which integrate SDDA as an intermittency effect and account for local imbalance, possess the essential elements for a successful phenomenological representation of imbalanced MHD turbulence. This assertion stems from several key observations: firstly, the models provide scaling predictions for higher-order moments in the perpendicular component of the magnetic field that align well with our in-situ observations. Secondly, an inverse relationship between alignment angles and the intensity of field gradients suggests that the alignment mechanism originates from the mutual shearing of fields during imbalanced collisions of wavepackets. However, it’s worth noting that certain aspects of solar wind turbulence, such as the presence of two sub-inertial ranges and anisotropic signatures, remain unaddressed by the models. This suggests that incorporating additional effects, such as accounting for inhomogeneity or the spherical polarization of fluctuations, could enhance the models’ scaling predictions.

1 N.S. acknowledges useful conversations with Michael
 2 Stevens about the use of SPC data. We acknowl-
 3 edge PSP/FIELDS team (PI: Stuart D. Bale, UC
 4 Berkeley) and PSP/SWEAP team (PI: Justin Kasper,
 5 BWX Technologies) for the use of data. This re-
 6 search was funded in part by the FIELDS experiment
 7 on the Parker Solar Probe spacecraft, designed and
 8 developed under NASA contract NNN06AA01C; the
 9 NASA Parker Solar Probe Observatory Scientist grant
 10 NNX15AF34G and the HERMES DRIVE NASA Sci-
 11 ence Center grant No. 80NSSC20K0604. The instru-
 12 ments of PSP were designed and developed under NASA
 13 contract NNN06AA01C. BC acknowledges the support
 14 of NASA grant 80NSSC24K0171.

Software: Python (Van Rossum & Drake Jr 1995), SciPy (Virtanen et al. 2020), Pandas (McKinney et al. 2010), Matplotlib (Hunter 2007), Pyspedas (Angelopoulos et al. 2019), (Sioulas 2023)

REFERENCES

- Alexandrova, O., Carbone, V., Veltri, P., & Sorriso-Valvo, L. 2008, *ApJ*, 674, 1153, doi: [10.1086/524056](https://doi.org/10.1086/524056)
- Alfvén, H. 1942, *Nature*, 150, 405, doi: [10.1038/150405d0](https://doi.org/10.1038/150405d0)
- Andrés, N., Sahraoui, F., Galtier, S., et al. 2019, *Phys. Rev. Lett.*, 123, 245101, doi: [10.1103/PhysRevLett.123.245101](https://doi.org/10.1103/PhysRevLett.123.245101)
- Angelopoulos, V., Cruce, P., Drozdov, A., et al. 2019, *Space Science Reviews*, 215, 9, doi: [10.1007/s11214-018-0576-4](https://doi.org/10.1007/s11214-018-0576-4)
- Bale, S. D., Goetz, K., Harvey, P. R., et al. 2016, *fr*, 204, 49, doi: [10.1007/s11214-016-0244-5](https://doi.org/10.1007/s11214-016-0244-5)
- Bale, S. D., Badman, S. T., Bonnell, J. W., et al. 2019, *Nature*, 1, doi: [10.1038/s41586-019-1818-7](https://doi.org/10.1038/s41586-019-1818-7)
- Barnes, A., & Hollweg, J. V. 1974, *Journal of Geophysical Research (1896-1977)*, 79, 2302, doi: <https://doi.org/10.1029/JA079i016p02302>
- Batchelor, G. K., Townsend, A. A., & Jeffreys, H. 1949, *Proceedings of the Royal Society of London. Series A. Mathematical and Physical Sciences*, 199, 238, doi: [10.1098/rspa.1949.0136](https://doi.org/10.1098/rspa.1949.0136)
- Beresnyak, A. 2011, *Phys. Rev. Lett.*, 106, 075001, doi: [10.1103/PhysRevLett.106.075001](https://doi.org/10.1103/PhysRevLett.106.075001)
- Beresnyak, A. 2012, *MNRAS*, 422, 3495, doi: [10.1111/j.1365-2966.2012.20859.x](https://doi.org/10.1111/j.1365-2966.2012.20859.x)
- . 2014, *ApJL*, 784, L20, doi: [10.1088/2041-8205/784/2/L20](https://doi.org/10.1088/2041-8205/784/2/L20)
- . 2015, *ApJL*, 801, L9, doi: [10.1088/2041-8205/801/1/L9](https://doi.org/10.1088/2041-8205/801/1/L9)
- Beresnyak, A., & Lazarian, A. 2006, *ApJL*, 640, L175, doi: [10.1086/503708](https://doi.org/10.1086/503708)
- . 2008, *ApJ*, 682, 1070, doi: [10.1086/589428](https://doi.org/10.1086/589428)
- . 2009, *ApJ*, 702, 1190, doi: [10.1088/0004-637X/702/2/1190](https://doi.org/10.1088/0004-637X/702/2/1190)
- Biskamp, D. 2003, *Magnetohydrodynamic Turbulence*
- Boldyrev, S. 2002, *ApJ*, 569, 841, doi: [10.1086/339403](https://doi.org/10.1086/339403)
- Boldyrev, S. 2005, *The Astrophysical Journal*, 626, L37, doi: [10.1086/431649](https://doi.org/10.1086/431649)
- . 2006, *Phys. Rev. Lett.*, 96, 115002, doi: [10.1103/PhysRevLett.96.115002](https://doi.org/10.1103/PhysRevLett.96.115002)
- Boldyrev, S., & Loureiro, N. F. 2017, *The Astrophysical Journal*, 844, 125, doi: [10.3847/1538-4357/aa7d02](https://doi.org/10.3847/1538-4357/aa7d02)
- Boldyrev, S., & Perez, J. C. 2012, *The Astrophysical Journal Letters*, 758, L44, doi: [10.1088/2041-8205/758/2/L44](https://doi.org/10.1088/2041-8205/758/2/L44)
- Bourouaine, S., Perez, J. C., Klein, K. G., et al. 2020, *ApJL*, 904, L30, doi: [10.3847/2041-8213/abbd4a](https://doi.org/10.3847/2041-8213/abbd4a)
- Bowen, T. A., Mallet, A., Bonnell, J. W., & Bale, S. D. 2018, *ApJ*, 865, 45, doi: [10.3847/1538-4357/aad95b](https://doi.org/10.3847/1538-4357/aad95b)
- Bowen, T. A., Bale, S. D., Bonnell, J. W., et al. 2020, *Journal of Geophysical Research: Space Physics*, 125, e2020JA027813, doi: <https://doi.org/10.1029/2020JA027813>
- Bowen, T. A., Mallet, A., Bale, S. D., et al. 2020a, *PhRvL*, 125, 025102, doi: [10.1103/PhysRevLett.125.025102](https://doi.org/10.1103/PhysRevLett.125.025102)
- Bowen, T. A., Mallet, A., Huang, J., et al. 2020b, *ApJS*, 246, 66, doi: [10.3847/1538-4365/ab6c65](https://doi.org/10.3847/1538-4365/ab6c65)
- Bowen, T. A., Badman, S. T., Bale, S. D., et al. 2021, *Nonlinear Interactions in Spherically Polarized Alfvénic Turbulence*. <https://arxiv.org/abs/2110.11454>
- Bowen, T. A., Bale, S. D., Chandran, B. D. G., et al. 2023, *Mediation of Collisionless Turbulent Dissipation Through Cyclotron Resonance*. <https://arxiv.org/abs/2306.04881>
- Bruno, R., & Carbone, V. 2013, *Living Reviews in Solar Physics*, 10, 2, doi: [10.12942/lrsp-2013-2](https://doi.org/10.12942/lrsp-2013-2)
- Bruno, R., Carbone, V., Sorriso-Valvo, L., & Bavassano, B. 2003, *Journal of Geophysical Research (Space Physics)*, 108, 1130, doi: [10.1029/2002JA009615](https://doi.org/10.1029/2002JA009615)
- Bruno, R., Carbone, V., Veltri, P., Pietropaolo, E., & Bavassano, B. 2001, *Planet. Space Sci.*, 49, 1201, doi: [10.1016/S0032-0633\(01\)00061-7](https://doi.org/10.1016/S0032-0633(01)00061-7)
- Burlaga, L. F. 1991, *J. Geophys. Res.*, 96, 5847, doi: [10.1029/91JA00087](https://doi.org/10.1029/91JA00087)
- Butterworth, S. 1930, *From 1923 to 1930, the journal was called Experimental Wireless and the Radio Engineer*, 7, 536. <https://cir.nii.ac.jp/crid/1572261550684507392>
- Cerri, S. S., & Califano, F. 2017, *New Journal of Physics*, 19, 025007, doi: [10.1088/1367-2630/aa5c4a](https://doi.org/10.1088/1367-2630/aa5c4a)
- Cerri, S. S., Grošelj, D., & Franci, L. 2019, *Frontiers in Astronomy and Space Sciences*, 6, 64, doi: [10.3389/fspas.2019.00064](https://doi.org/10.3389/fspas.2019.00064)
- Cerri, S. S., Passot, T., Laveder, D., Sulem, P. L., & Kunz, M. W. 2022, *ApJ*, 939, 36, doi: [10.3847/1538-4357/ac93fe](https://doi.org/10.3847/1538-4357/ac93fe)
- Chandran, B. D. G. 2005, *PhRvL*, 95, 265004, doi: [10.1103/PhysRevLett.95.265004](https://doi.org/10.1103/PhysRevLett.95.265004)
- . 2008, *ApJ*, 685, 646, doi: [10.1086/589432](https://doi.org/10.1086/589432)
- Chandran, B. D. G. 2018, *Journal of Plasma Physics*, 84, 905840106, doi: [10.1017/S0022377818000016](https://doi.org/10.1017/S0022377818000016)
- Chandran, B. D. G., & Perez, J. C. 2019, *Journal of Plasma Physics*, 85, 905850409, doi: [10.1017/S0022377819000540](https://doi.org/10.1017/S0022377819000540)
- Chandran, B. D. G., Schekochihin, A. A., & Mallet, A. 2015, *ApJ*, 807, 39, doi: [10.1088/0004-637X/807/1/39](https://doi.org/10.1088/0004-637X/807/1/39)
- Chandran, B. D. G., Schekochihin, A. A., & Mallet, A. 2015, *The Astrophysical Journal*, 807, 39, doi: [10.1088/0004-637X/807/1/39](https://doi.org/10.1088/0004-637X/807/1/39)
- Chen, C. H. K. 2016, *Journal of Plasma Physics*, 82, 535820602, doi: [10.1017/S0022377816001124](https://doi.org/10.1017/S0022377816001124)
- Chen, C. H. K., Bale, S. D., Salem, C. S., & Maruca, B. A. 2013, *The Astrophysical Journal*, 770, 125, doi: [10.1088/0004-637X/770/2/125](https://doi.org/10.1088/0004-637X/770/2/125)
- Chen, C. H. K., Mallet, A., Schekochihin, A. A., et al. 2012, *ApJ*, 758, 120, doi: [10.1088/0004-637X/758/2/120](https://doi.org/10.1088/0004-637X/758/2/120)

- Chen, C. H. K., Mallet, A., Yousef, T. A., Schekochihin, A. A., & Horbury, T. S. 2011, *MNRAS*, 415, 3219, doi: [10.1111/j.1365-2966.2011.18933.x](https://doi.org/10.1111/j.1365-2966.2011.18933.x)
- Chen, C. H. K., Sorriso-Valvo, L., Šafránková, J., & Němeček, Z. 2014, *ApJL*, 789, L8, doi: [10.1088/2041-8205/789/1/L8](https://doi.org/10.1088/2041-8205/789/1/L8)
- Chhiber, R., Matthaeus, W. H., Bowen, T. A., & Bale, S. D. 2021, *ApJL*, 911, L7, doi: [10.3847/2041-8213/abf04e](https://doi.org/10.3847/2041-8213/abf04e)
- Chhiber, R., Matthaeus, W. H., Oughton, S., & Parashar, T. N. 2020, *Physics of Plasmas*, 27, 062308, doi: [10.1063/5.0005109](https://doi.org/10.1063/5.0005109)
- Chhiber, R., Goldstein, M. L., Maruca, B. A., et al. 2020, *The Astrophysical Journal Supplement Series*, 246, 31, doi: [10.3847/1538-4365/ab53d2](https://doi.org/10.3847/1538-4365/ab53d2)
- Cho, J. 2019, *ApJ*, 874, 75, doi: [10.3847/1538-4357/ab06f3](https://doi.org/10.3847/1538-4357/ab06f3)
- Cho, J., & Lazarian, A. 2003, *MNRAS*, 345, 325, doi: [10.1046/j.1365-8711.2003.06941.x](https://doi.org/10.1046/j.1365-8711.2003.06941.x)
- Cho, J., & Vishniac, E. T. 2000, *ApJ*, 539, 273, doi: [10.1086/309213](https://doi.org/10.1086/309213)
- Comisso, L., Huang, Y. M., Lingam, M., Hirvijoki, E., & Bhattacharjee, A. 2018, *ApJ*, 854, 103, doi: [10.3847/1538-4357/aaac83](https://doi.org/10.3847/1538-4357/aaac83)
- Coppi, B., Galvao, R., Pellat, R., Rosenbluth, M., & Rutherford, P. 1976, *Soviet Journal of Plasma Physics*, 2, 533
- Cuesta, M. E., Chhiber, R., Roy, S., et al. 2022, *ApJL*, 932, L11, doi: [10.3847/2041-8213/ac73fd](https://doi.org/10.3847/2041-8213/ac73fd)
- D'Amicis, R., Alielden, K., Perrone, D., et al. 2021, *A&A*, 654, A111, doi: [10.1051/0004-6361/202140600](https://doi.org/10.1051/0004-6361/202140600)
- D'Amicis, R., Perrone, D., Velli, M., et al. 2022, *Universe*, 8, 352, doi: [10.3390/universe8070352](https://doi.org/10.3390/universe8070352)
- Davis, N., Chandran, B. D. G., Bowen, T. A., et al. 2023, *ApJ*, 950, 154, doi: [10.3847/1538-4357/acd177](https://doi.org/10.3847/1538-4357/acd177)
- Dmitruk, P., Matthaeus, W. H., & Oughton, S. 2005, *Physics of Plasmas*, 12, 112304, doi: [10.1063/1.2128573](https://doi.org/10.1063/1.2128573)
- Dobrowolny, M., Mangeney, A., & Veltri, P. 1980, *Phys. Rev. Lett.*, 45, 144, doi: [10.1103/PhysRevLett.45.144](https://doi.org/10.1103/PhysRevLett.45.144)
- Dong, C., Wang, L., Huang, Y.-M., et al. 2022, *Science Advances*, 8, eabn7627, doi: [10.1126/sciadv.abn7627](https://doi.org/10.1126/sciadv.abn7627)
- Dong, Y., Verdini, A., & Grappin, R. 2014, *The Astrophysical Journal*, 793, 118, doi: [10.1088/0004-637X/793/2/118](https://doi.org/10.1088/0004-637X/793/2/118)
- Duan, D., He, J., Bowen, T. A., et al. 2021, *The Astrophysical Journal Letters*, 915, L8, doi: [10.3847/2041-8213/ac07ac](https://doi.org/10.3847/2041-8213/ac07ac)
- Dudok de Wit, T., Alexandrova, O., Furno, I., Sorriso-Valvo, L., & Zimbardo, G. 2013, *SSRv*, 178, 665, doi: [10.1007/s11214-013-9974-9](https://doi.org/10.1007/s11214-013-9974-9)
- Elsasser, W. M. 1950, *Phys. Rev.*, 79, 183, doi: [10.1103/PhysRev.79.183](https://doi.org/10.1103/PhysRev.79.183)
- Feller, W. 1968, *An Introduction to Probability Theory and Its Applications*, Vol. 1 (Wiley). <http://www.amazon.ca/exec/obidos/redirect?tag=citeulike04-20&path=ASIN/0471257087>
- Fox, N. J., Velli, M. C., Bale, S. D., et al. 2016, *fr*, 204, 7, doi: [10.1007/s11214-015-0211-6](https://doi.org/10.1007/s11214-015-0211-6)
- Franci, L., Cerri, S. S., Califano, F., et al. 2017, *ApJL*, 850, L16, doi: [10.3847/2041-8213/aa93fb](https://doi.org/10.3847/2041-8213/aa93fb)
- Franz, M., & Harper, D. 2002, *Planetary and Space Science*, 50, 217, doi: [https://doi.org/10.1016/S0032-0633\(01\)00119-2](https://doi.org/https://doi.org/10.1016/S0032-0633(01)00119-2)
- Frisch, U. 1995, *Turbulence: The Legacy of A.N. Kolmogorov*, doi: [10.1017/CBO9781139170666](https://doi.org/10.1017/CBO9781139170666)
- Frisch, U., Sulem, P. L., & Nelkin, M. 1978, *Journal of Fluid Mechanics*, 87, 719, doi: [10.1017/S0022112078001846](https://doi.org/10.1017/S0022112078001846)
- Furth, H. P., Killeen, J., & Rosenbluth, M. N. 1963, *The Physics of Fluids*, 6, 459, doi: [10.1063/1.1706761](https://doi.org/10.1063/1.1706761)
- Galtier, S., Nazarenko, S. V., Newell, A. C., & Pouquet, A. 2000, *Journal of Plasma Physics*, 63, 447, doi: [10.1017/S0022377899008284](https://doi.org/10.1017/S0022377899008284)
- Gerick, F., Saur, J., & von Papen, M. 2017, *The Astrophysical Journal*, 843, 5, doi: [10.3847/1538-4357/aa767c](https://doi.org/10.3847/1538-4357/aa767c)
- Goldreich, P., & Sridhar, S. 1995, *apj*, 438, 763, doi: [10.1086/175121](https://doi.org/10.1086/175121)
- Goldstein, M. L., Roberts, D. A., & Matthaeus, W. H. 1989, *Geophysical Monograph Series*, 54, 113, doi: [10.1029/GM054p0113](https://doi.org/10.1029/GM054p0113)
- Grappin, R. 1986, *Physics of Fluids*, 29, 2433, doi: [10.1063/1.865536](https://doi.org/10.1063/1.865536)
- Grappin, R., & Velli, M. 1996, *J. Geophys. Res.*, 101, 425, doi: [10.1029/95JA02147](https://doi.org/10.1029/95JA02147)
- Grappin, R., Velli, M., & Mangeney, A. 1993, *Phys. Rev. Lett.*, 70, 2190, doi: [10.1103/PhysRevLett.70.2190](https://doi.org/10.1103/PhysRevLett.70.2190)
- Grappin, R., Verdini, A., & Müller, W.-C. 2022, *The Astrophysical Journal*, 933, 246
- Grauer, R., Krug, J. H. A., & Marliani, C. 1994, *Physics Letters A*, 195, 335
- Greco, A., Matthaeus, W. H., Perri, S., et al. 2018, *fr*, 214, 1, doi: [10.1007/s11214-017-0435-8](https://doi.org/10.1007/s11214-017-0435-8)
- Gurland, J., & Tripathi, R. C. 1971, *The American Statistician*, 25, 30. <http://www.jstor.org/stable/2682923>
- Higdon, J. C. 1984, *ApJ*, 285, 109, doi: [10.1086/162481](https://doi.org/10.1086/162481)
- Hnat, B., Chapman, S. C., Gogoberidze, G., & Wicks, R. T. 2011, *Phys. Rev. E*, 84, 065401, doi: [10.1103/PhysRevE.84.065401](https://doi.org/10.1103/PhysRevE.84.065401)

- Hollweg, J. V., & Isenberg, P. A. 2007, *Journal of Geophysical Research: Space Physics*, 112, doi: <https://doi.org/10.1029/2007JA012253>
- Horbury, T. S., & Balogh, A. 1997a, *Nonlinear Processes in Geophysics*, 4, 185, doi: [10.5194/npg-4-185-1997](https://doi.org/10.5194/npg-4-185-1997)
- . 1997b, *Nonlinear Processes in Geophysics*, 4, 185, doi: [10.5194/npg-4-185-1997](https://doi.org/10.5194/npg-4-185-1997)
- . 2001, *J. Geophys. Res.*, 106, 15929, doi: [10.1029/2000JA000108](https://doi.org/10.1029/2000JA000108)
- Horbury, T. S., Forman, M., & Oughton, S. 2008, *\prl*, 101, 175005, doi: [10.1103/PhysRevLett.101.175005](https://doi.org/10.1103/PhysRevLett.101.175005)
- Horbury, T. S., Matteini, L., & Stansby, D. 2018, *MNRAS*, 478, 1980, doi: [10.1093/mnras/sty953](https://doi.org/10.1093/mnras/sty953)
- Horbury, T. S., Bale, S. D., McManus, M. D., et al. 2023, *Physics of Plasmas*, 30, 082905, doi: [10.1063/5.0123250](https://doi.org/10.1063/5.0123250)
- Howes, G. G. 2015, *Philosophical Transactions of the Royal Society A: Mathematical, Physical and Engineering Sciences*, 373, 20140145, doi: [10.1098/rsta.2014.0145](https://doi.org/10.1098/rsta.2014.0145)
- Howes, G. G., Bale, S. D., Klein, K. G., et al. 2012, *\apjl*, 753, L19, doi: [10.1088/2041-8205/753/1/L19](https://doi.org/10.1088/2041-8205/753/1/L19)
- Howes, G. G., Cowley, S. C., Dorland, W., et al. 2008, *Journal of Geophysical Research (Space Physics)*, 113, A05103, doi: [10.1029/2007JA012665](https://doi.org/10.1029/2007JA012665)
- Huang, Z., Sioulas, N., Shi, C., et al. 2023, *ApJL*, 950, L8, doi: [10.3847/2041-8213/acd7f2](https://doi.org/10.3847/2041-8213/acd7f2)
- Hunter, J. D. 2007, *Computing in Science & Engineering*, 9, 90, doi: [10.1109/MCSE.2007.55](https://doi.org/10.1109/MCSE.2007.55)
- Iroshnikov, P. S. 1963, *Astronomicheskii Zhurnal*, 40, 742. <https://ui.adsabs.harvard.edu/abs/1963AZh....40..742I>
- Kadomtsev, B. B., & Pogutse, O. P. 1967, *Soviet Journal of Experimental and Theoretical Physics*, 24, 1172
- Kasper, J. C., Abiad, R., Austin, G., et al. 2016, *\br*, 204, 131, doi: [10.1007/s11214-015-0206-3](https://doi.org/10.1007/s11214-015-0206-3)
- Klein, K. G., Howes, G. G., TenBarge, J. M., et al. 2012, *ApJ*, 755, 159, doi: [10.1088/0004-637X/755/2/159](https://doi.org/10.1088/0004-637X/755/2/159)
- Kolmogorov, A. 1941, *Akademiia Nauk SSSR Doklady*, 30, 301
- Kolmogorov, A. N. 1962, *Journal of Fluid Mechanics*, 13, 82, doi: [10.1017/S0022112062000518](https://doi.org/10.1017/S0022112062000518)
- Kraichnan, R. H. 1965, *The Physics of Fluids*, 8, 1385
- Landau, L. D., & Lifshitz, E. M. 1959, *Fluid mechanics*
- Lithwick, Y., Goldreich, P., & Sridhar, S. 2007, *ApJ*, 655, 269, doi: [10.1086/509884](https://doi.org/10.1086/509884)
- Loureiro, N. F., & Boldyrev, S. 2017, *PhRvL*, 118, 245101, doi: [10.1103/PhysRevLett.118.245101](https://doi.org/10.1103/PhysRevLett.118.245101)
- Malagoli, A., Bodo, G., & Rosner, R. 1996, *ApJ*, 456, 708, doi: [10.1086/176691](https://doi.org/10.1086/176691)
- Mallet, A., & Schekochihin, A. A. 2017, *MNRAS*, 466, 3918, doi: [10.1093/mnras/stw3251](https://doi.org/10.1093/mnras/stw3251)
- Mallet, A., Schekochihin, A. A., & Chandran, B. D. G. 2015, *MNRAS*, 449, L77, doi: [10.1093/mnrasl/slv021](https://doi.org/10.1093/mnrasl/slv021)
- Mallet, A., Schekochihin, A. A., & Chandran, B. D. G. 2017, *Journal of Plasma Physics*, 83, 905830609, doi: [10.1017/S0022377817000812](https://doi.org/10.1017/S0022377817000812)
- Mallet, A., Schekochihin, A. A., Chandran, B. D. G., et al. 2016, *MNRAS*, 459, 2130, doi: [10.1093/mnras/stw802](https://doi.org/10.1093/mnras/stw802)
- Mallet, A., Squire, J., Chandran, B. D. G., Bowen, T., & Bale, S. D. 2021, *ApJ*, 918, 62, doi: [10.3847/1538-4357/ac0c12](https://doi.org/10.3847/1538-4357/ac0c12)
- Mangeney, A. 2001, in *ESA Special Publication*, Vol. 492, *Sheffield Space Plasma Meeting: Multipoint Measurements versus Theory*, ed. B. Warmbein, 53
- Maron, J., & Goldreich, P. 2001, *ApJ*, 554, 1175, doi: [10.1086/321413](https://doi.org/10.1086/321413)
- Mason, J., Cattaneo, F., & Boldyrev, S. 2006, *Phys. Rev. Lett.*, 97, 255002, doi: [10.1103/PhysRevLett.97.255002](https://doi.org/10.1103/PhysRevLett.97.255002)
- Matteini, L., Horbury, T. S., Neugebauer, M., & Goldstein, B. E. 2014, *Geophysical Research Letters*, 41, 259, doi: <https://doi.org/10.1002/2013GL058482>
- Matteini, L., Tenerani, A., Landi, S., et al. 2024, *Physics of Plasmas*, 31, 032901, doi: [10.1063/5.0177754](https://doi.org/10.1063/5.0177754)
- Matthaeus, W. H., Pouquet, A., Mininni, P. D., Dmitruk, P., & Breech, B. 2008, *Phys. Rev. Lett.*, 100, 085003, doi: [10.1103/PhysRevLett.100.085003](https://doi.org/10.1103/PhysRevLett.100.085003)
- Matthaeus, W. H., Servidio, S., Dmitruk, P., et al. 2012, *ApJ*, 750, 103, doi: [10.1088/0004-637X/750/2/103](https://doi.org/10.1088/0004-637X/750/2/103)
- Matthaeus, W. H., & Velli, M. 2011, *Space Science Reviews*, 160, 145, doi: [10.1007/s11214-011-9793-9](https://doi.org/10.1007/s11214-011-9793-9)
- McIntyre, J. R., Chen, C. H. K., & Larosa, A. 2023, *The Astrophysical Journal*, 957, 111, doi: [10.3847/1538-4357/acf3dd](https://doi.org/10.3847/1538-4357/acf3dd)
- McKinney, W., et al. 2010, in *Proceedings of the 9th Python in Science Conference*, Vol. 445, Austin, TX, 51–56
- Meyrand, R., Galtier, S., & Kiyani, K. H. 2016, *Phys. Rev. Lett.*, 116, 105002, doi: [10.1103/PhysRevLett.116.105002](https://doi.org/10.1103/PhysRevLett.116.105002)
- Meyrand, R., Squire, J., Mallet, A., & Chandran, B. D. G. 2023, *Reflection-driven turbulence in the super-Alfvénic solar wind*. <https://arxiv.org/abs/2308.10389>
- Meyrand, R., Squire, J., Schekochihin, A., & Dorland, W. 2021, *Journal of Plasma Physics*, 87, 535870301, doi: [10.1017/S0022377821000489](https://doi.org/10.1017/S0022377821000489)
- Moncuquet, M., Meyer-Vernet, N., Issautier, K., et al. 2020, *The Astrophysical Journal Supplement Series*, 246, 44, doi: [10.3847/1538-4365/ab5a84](https://doi.org/10.3847/1538-4365/ab5a84)
- Monin, A. S., & Jaglom, A. M. 1987, *Statistical fluid mechanics*. 2, 3rd edn. (Cambridge, Mass.: MIT Pr)
- Montgomery, D., & Turner, L. 1981, *Physics of Fluids*, 24, 825, doi: [10.1063/1.863455](https://doi.org/10.1063/1.863455)

- Müller, W.-C., & Biskamp, D. 2000, *Phys. Rev. Lett.*, 84, 475, doi: [10.1103/PhysRevLett.84.475](https://doi.org/10.1103/PhysRevLett.84.475)
- Müller, W.-C., Biskamp, D., & Grappin, R. 2003, *PhRvE*, 67, 066302, doi: [10.1103/PhysRevE.67.066302](https://doi.org/10.1103/PhysRevE.67.066302)
- Müller, W.-C., & Grappin, R. 2005, *Phys. Rev. Lett.*, 95, 114502, doi: [10.1103/PhysRevLett.95.114502](https://doi.org/10.1103/PhysRevLett.95.114502)
- Ng, C. S., & Bhattacharjee, A. 1996, *ApJ*, 465, 845, doi: [10.1086/177468](https://doi.org/10.1086/177468)
- Oboukhov, A. M. 1962, *Journal of Fluid Mechanics*, 13, 77, doi: [10.1017/S0022112062000506](https://doi.org/10.1017/S0022112062000506)
- Osman, K. T., Matthaeus, W. H., Wan, M., & Rappazzo, A. F. 2012, *Phys. Rev. Lett.*, 108, 261102, doi: [10.1103/PhysRevLett.108.261102](https://doi.org/10.1103/PhysRevLett.108.261102)
- Oughton, S., & Matthaeus, W. H. 2020, *ApJ*, 897, 37, doi: [10.3847/1538-4357/ab8f2a](https://doi.org/10.3847/1538-4357/ab8f2a)
- Oughton, S., Matthaeus, W. H., & Dmitruk, P. 2017, *ApJ*, 839, 2, doi: [10.3847/1538-4357/aa67e2](https://doi.org/10.3847/1538-4357/aa67e2)
- Oughton, S., Matthaeus, W. H., & Dmitruk, P. 2017, *The Astrophysical Journal*, 839, 2, doi: [10.3847/1538-4357/aa67e2](https://doi.org/10.3847/1538-4357/aa67e2)
- Palacios, J. C., Bourouaine, S., & Perez, J. C. 2022, *ApJL*, 940, L20, doi: [10.3847/2041-8213/ac92f6](https://doi.org/10.3847/2041-8213/ac92f6)
- Parashar, T. N., Cuesta, M., & Matthaeus, W. H. 2019, *The Astrophysical Journal*, 884, L57, doi: [10.3847/2041-8213/ab4a82](https://doi.org/10.3847/2041-8213/ab4a82)
- Parashar, T. N., Goldstein, M. L., Maruca, B. A., et al. 2020, *The Astrophysical Journal Supplement Series*, 246, 58, doi: [10.3847/1538-4365/ab64e6](https://doi.org/10.3847/1538-4365/ab64e6)
- Parker, E. N., & Tidman, D. A. 1958, *Physical Review*, 111, 1206, doi: [10.1103/PhysRev.111.1206](https://doi.org/10.1103/PhysRev.111.1206)
- Passot, T., & Sulem, P. L. 2019, *Journal of Plasma Physics*, 85, 905850301, doi: [10.1017/S0022377819000187](https://doi.org/10.1017/S0022377819000187)
- Passot, T., Sulem, P. L., & Laveder, D. 2022, *Journal of Plasma Physics*, 88, 905880312, doi: [10.1017/S0022377822000472](https://doi.org/10.1017/S0022377822000472)
- Passot, T., Sulem, P. L., & Tassi, E. 2018, *Physics of Plasmas*, 25, 042107, doi: [10.1063/1.5022528](https://doi.org/10.1063/1.5022528)
- Perez, J. C., & Boldyrev, S. 2009, *Phys. Rev. Lett.*, 102, 025003, doi: [10.1103/PhysRevLett.102.025003](https://doi.org/10.1103/PhysRevLett.102.025003)
- Perez, J. C., & Chandran, B. D. G. 2013, *The Astrophysical Journal*, 776, 124, doi: [10.1088/0004-637X/776/2/124](https://doi.org/10.1088/0004-637X/776/2/124)
- Perez, J. C., Mason, J., Boldyrev, S., & Cattaneo, F. 2012, *Phys. Rev. X*, 2, 041005, doi: [10.1103/PhysRevX.2.041005](https://doi.org/10.1103/PhysRevX.2.041005)
- . 2014, *The Astrophysical Journal Letters*, 793, L13, doi: [10.1088/2041-8205/793/1/L13](https://doi.org/10.1088/2041-8205/793/1/L13)
- Podesta, J. J. 2009, *The Astrophysical Journal*, 698, 986, doi: [10.1088/0004-637x/698/2/986](https://doi.org/10.1088/0004-637x/698/2/986)
- Podesta, J. J., & Bhattacharjee, A. 2010, *ApJ*, 718, 1151, doi: [10.1088/0004-637X/718/2/1151](https://doi.org/10.1088/0004-637X/718/2/1151)
- Podesta, J. J., & Borovsky, J. E. 2010, *Physics of Plasmas*, 17, 112905, doi: [10.1063/1.3505092](https://doi.org/10.1063/1.3505092)
- Podesta, J. J., Chandran, B. D. G., Bhattacharjee, A., Roberts, D. A., & Goldstein, M. L. 2009, *Journal of Geophysical Research (Space Physics)*, 114, A01107, doi: [10.1029/2008JA013504](https://doi.org/10.1029/2008JA013504)
- Politano, H., & Pouquet, A. 1995, *Phys. Rev. E*, 52, 636, doi: [10.1103/PhysRevE.52.636](https://doi.org/10.1103/PhysRevE.52.636)
- Pucci, F., & Velli, M. 2014, *ApJL*, 780, L19, doi: [10.1088/2041-8205/780/2/L19](https://doi.org/10.1088/2041-8205/780/2/L19)
- Pulupa, M., Bale, S. D., Bonnell, J. W., et al. 2017, *Journal of Geophysical Research: Space Physics*, 122, 2836, doi: [10.1002/2016JA023345](https://doi.org/10.1002/2016JA023345)
- Roberts, D. A., Goldstein, M. L., Klein, L. W., & Matthaeus, W. H. 1987, *Journal of Geophysical Research: Space Physics*, 92, 12023, doi: [https://doi.org/10.1029/JA092iA11p12023](https://doi.org/https://doi.org/10.1029/JA092iA11p12023)
- Roberts, D. A., Goldstein, M. L., Matthaeus, W. H., & Ghosh, S. 1992, *Jgr*, 97, 17115, doi: [10.1029/92JA01144](https://doi.org/10.1029/92JA01144)
- Ruffolo, D., Matthaeus, W. H., Chhiber, R., et al. 2020, *ApJ*, 902, 94, doi: [10.3847/1538-4357/abb594](https://doi.org/10.3847/1538-4357/abb594)
- Ruzmaikin, A. A., Feynman, J., Goldstein, B. E., Smith, E. J., & Balogh, A. 1995, *J. Geophys. Res.*, 100, 3395, doi: [10.1029/94JA02808](https://doi.org/10.1029/94JA02808)
- Sahraoui, F., Goldstein, M. L., Robert, P., & Khotyaintsev, Y. V. 2009, *PhRvL*, 102, 231102, doi: [10.1103/PhysRevLett.102.231102](https://doi.org/10.1103/PhysRevLett.102.231102)
- Salem, C., Mangeney, A., Bale, S. D., & Veltri, P. 2009, *ApJ*, 702, 537, doi: [10.1088/0004-637X/702/1/537](https://doi.org/10.1088/0004-637X/702/1/537)
- Schekochihin, A. A. 2022, *Journal of Plasma Physics*, 88, 155880501, doi: [10.1017/S0022377822000721](https://doi.org/10.1017/S0022377822000721)
- Schekochihin, A. A., Cowley, S. C., Dorland, W., et al. 2009a, *apjs*, 182, 310, doi: [10.1088/0067-0049/182/1/310](https://doi.org/10.1088/0067-0049/182/1/310)
- . 2009b, *The Astrophysical Journal Supplement Series*, 182, 310, doi: [10.1088/0067-0049/182/1/310](https://doi.org/10.1088/0067-0049/182/1/310)
- Shankarappa, N., Klein, K. G., & Martinović, M. M. 2023, *The Astrophysical Journal*, 946, 85, doi: [10.3847/1538-4357/acb542](https://doi.org/10.3847/1538-4357/acb542)
- She, Z.-S., & Leveque, E. 1994, *PhRvL*, 72, 336, doi: [10.1103/PhysRevLett.72.336](https://doi.org/10.1103/PhysRevLett.72.336)
- Shebalin, J. V., Matthaeus, W. H., & Montgomery, D. 1983, *Journal of Plasma Physics*, 29, 525–547, doi: [10.1017/S0022377800000933](https://doi.org/10.1017/S0022377800000933)
- Shi, C., Sioulas, N., Huang, Z., et al. 2023, arXiv e-prints, arXiv:2308.12376, doi: [10.48550/arXiv.2308.12376](https://doi.org/10.48550/arXiv.2308.12376)
- Sioulas, N. 2023, *MHDTurbPy*, 0.1.0, Zenodo, doi: [10.5281/zenodo.7572468](https://doi.org/10.5281/zenodo.7572468)
- Sioulas, N., Huang, Z., Velli, M., et al. 2022, *The Astrophysical Journal*, 934, 143, doi: [10.3847/1538-4357/ac7aa2](https://doi.org/10.3847/1538-4357/ac7aa2)

- Sioulas, N., Velli, M., Huang, Z., et al. 2023, *The Astrophysical Journal*, 951, 141, doi: [10.3847/1538-4357/acc658](https://doi.org/10.3847/1538-4357/acc658)
- Sioulas, N., Huang, Z., Shi, C., et al. 2023, *ApJL*, 943, L8, doi: [10.3847/2041-8213/acaeff](https://doi.org/10.3847/2041-8213/acaeff)
- Soni, S. L., Akhavan-Tafti, M., Suen, G. H. H., et al. 2024, *Switchback Patches Evolve into Microstreams via Magnetic Relaxation*. <https://arxiv.org/abs/2402.13964>
- Sorriso-Valvo, L., Carbone, V., Veltri, P., Consolini, G., & Bruno, R. 1999, *Geophysical Research Letters*, 26, 1801, doi: <https://doi.org/10.1029/1999GL900270>
- Sorriso-Valvo, L., Marino, R., Foldes, R., et al. 2023, *A&A*, 672, A13, doi: [10.1051/0004-6361/202244889](https://doi.org/10.1051/0004-6361/202244889)
- Sorriso-Valvo, L., Yordanova, E., Dimmock, A. P., & Telloni, D. 2021, *The Astrophysical Journal Letters*, 919, L30, doi: [10.3847/2041-8213/ac26c5](https://doi.org/10.3847/2041-8213/ac26c5)
- Squire, J., Chandran, B. D. G., & Meyrand, R. 2020, *The Astrophysical Journal Letters*, 891, L2, doi: [10.3847/2041-8213/ab74e1](https://doi.org/10.3847/2041-8213/ab74e1)
- Squire, J., Meyrand, R., Kunz, M. W., et al. 2022a, *Nature Astronomy*, 6, 715, doi: [10.1038/s41550-022-01624-z](https://doi.org/10.1038/s41550-022-01624-z)
- . 2022b, *Nature Astronomy*, 6, 715, doi: [10.1038/s41550-022-01624-z](https://doi.org/10.1038/s41550-022-01624-z)
- Stix, T. H. 1992, *Waves in plasmas*
- Strauss, H. R. 1976, *Physics of Fluids*, 19, 134, doi: [10.1063/1.861310](https://doi.org/10.1063/1.861310)
- Telloni, D. 2022, *Frontiers in Astronomy and Space Sciences*, 9, doi: [10.3389/fspas.2022.917393](https://doi.org/10.3389/fspas.2022.917393)
- Tenerani, A., Sioulas, N., Matteini, L., et al. 2021, *The Astrophysical Journal Letters*, 919, L31, doi: [10.3847/2041-8213/ac2606](https://doi.org/10.3847/2041-8213/ac2606)
- Tu, C. Y., & Marsch, E. 1995, *SSRv*, 73, 1, doi: [10.1007/BF00748891](https://doi.org/10.1007/BF00748891)
- Tu, C. Y., Marsch, E., & Rosenbauer, H. 1990, *Geophys. Res. Lett.*, 17, 283, doi: [10.1029/GL017i003p00283](https://doi.org/10.1029/GL017i003p00283)
- Turner, A. J., Gogoberidze, G., Chapman, S. C., Hnat, B., & Müller, W. C. 2011, *PhRvL*, 107, 095002, doi: [10.1103/PhysRevLett.107.095002](https://doi.org/10.1103/PhysRevLett.107.095002)
- Uzdensky, D. A., & Loureiro, N. F. 2016, *Phys. Rev. Lett.*, 116, 105003, doi: [10.1103/PhysRevLett.116.105003](https://doi.org/10.1103/PhysRevLett.116.105003)
- Van Rossum, G., & Drake Jr, F. L. 1995, *Python reference manual (Centrum voor Wiskunde en Informatica Amsterdam)*
- Vech, D., & Chen, C. H. K. 2016, *The Astrophysical Journal Letters*, 832, L16, doi: [10.3847/2041-8205/832/1/L16](https://doi.org/10.3847/2041-8205/832/1/L16)
- Vech, D., Mallet, A., Klein, K. G., & Kasper, J. C. 2018, *The Astrophysical Journal Letters*, 855, L27, doi: [10.3847/2041-8213/aab351](https://doi.org/10.3847/2041-8213/aab351)
- Velli, M. 1993, *A&A*, 270, 304
- Velli, M., Grappin, R., & Mangeney, A. 1989, *Physical Review Letters*, 63, 1807, doi: [10.1103/PhysRevLett.63.1807](https://doi.org/10.1103/PhysRevLett.63.1807)
- Velli, M., Grappin, R., & Mangeney, A. 1990, *Computer Physics Communications*, 59, 153, doi: [10.1016/0010-4655\(90\)90165-W](https://doi.org/10.1016/0010-4655(90)90165-W)
- Velli, M., Grappin, R., & Mangeney, A. 1991, *Geophysical & Astrophysical Fluid Dynamics*, 62, 101, doi: [10.1080/03091929108229128](https://doi.org/10.1080/03091929108229128)
- Verdini, A., & Grappin, R. 2012, *Phys. Rev. Lett.*, 109, 025004, doi: [10.1103/PhysRevLett.109.025004](https://doi.org/10.1103/PhysRevLett.109.025004)
- Verdini, A., & Grappin, R. 2015, *ApJL*, 808, L34, doi: [10.1088/2041-8205/808/2/L34](https://doi.org/10.1088/2041-8205/808/2/L34)
- Verdini, A., Grappin, R., Alexandrova, O., et al. 2019, *MNRAS*, 486, 3006, doi: [10.1093/mnras/stz1041](https://doi.org/10.1093/mnras/stz1041)
- Verdini, A., Grappin, R., Alexandrova, O., & Lion, S. 2018, *ApJ*, 853, 85, doi: [10.3847/1538-4357/aaa433](https://doi.org/10.3847/1538-4357/aaa433)
- Verdini, A., Velli, M., & Buchlin, E. 2009, *ApJL*, 700, L39, doi: [10.1088/0004-637X/700/1/L39](https://doi.org/10.1088/0004-637X/700/1/L39)
- Vinogradov, A., Alexandrova, O., Démoulin, P., et al. 2023, *Embedded coherent structures from MHD to sub-ion scales in turbulent solar wind at 0.17 au*. <https://arxiv.org/abs/2307.10478>
- Virtanen, P., Gommers, R., Oliphant, T. E., et al. 2020, *Nature Methods*, 17, 261, doi: [10.1038/s41592-019-0686-2](https://doi.org/10.1038/s41592-019-0686-2)
- Völk, H. J., & Aplers, W. 1973, *Ap&SS*, 20, 267, doi: [10.1007/BF00642204](https://doi.org/10.1007/BF00642204)
- Wang, T., He, J., Alexandrova, O., Dunlop, M., & Perrone, D. 2020, *ApJ*, 898, 91, doi: [10.3847/1538-4357/ab99ca](https://doi.org/10.3847/1538-4357/ab99ca)
- Wang, X., Huang, L., Wang, Y., & Yuan, H. 2023, *Universe*, 9, doi: [10.3390/universe9090399](https://doi.org/10.3390/universe9090399)
- Wang, Y., Chhiber, R., Adhikari, S., et al. 2022, *Strategies for determining the cascade rate in MHD turbulence: isotropy, anisotropy, and spacecraft sampling*, arXiv, doi: [10.48550/ARXIV.2209.00208](https://doi.org/10.48550/ARXIV.2209.00208)
- Wicks, R. T., Horbury, T. S., Chen, C. H. K., & Schekochihin, A. A. 2011, *PhRvL*, 106, 045001, doi: [10.1103/PhysRevLett.106.045001](https://doi.org/10.1103/PhysRevLett.106.045001)
- Wicks, R. T., Mallet, A., Horbury, T. S., et al. 2013a, *Phys. Rev. Lett.*, 110, 025003, doi: [10.1103/PhysRevLett.110.025003](https://doi.org/10.1103/PhysRevLett.110.025003)
- Wicks, R. T., Roberts, D. A., Mallet, A., et al. 2013b, *The Astrophysical Journal*, 778, 177, doi: [10.1088/0004-637X/778/2/177](https://doi.org/10.1088/0004-637X/778/2/177)
- Wu, H., He, J., Yang, L., et al. 2022, *On the scaling and anisotropy of two subranges in the inertial range of solar wind turbulence*, arXiv, doi: [10.48550/ARXIV.2209.12409](https://doi.org/10.48550/ARXIV.2209.12409)

- Wu, H., Huang, S., Wang, X., et al. 2023, *The Astrophysical Journal Letters*, 947, L22, doi: [10.3847/2041-8213/acca20](https://doi.org/10.3847/2041-8213/acca20)
- Wu, P., Perri, S., Osman, K., et al. 2013, *ApJL*, 763, L30, doi: [10.1088/2041-8205/763/2/L30](https://doi.org/10.1088/2041-8205/763/2/L30)
- Yao, S., He, J. S., Marsch, E., et al. 2011, *ApJ*, 728, 146, doi: [10.1088/0004-637X/728/2/146](https://doi.org/10.1088/0004-637X/728/2/146)
- Zhang, J., Huang, S. Y., He, J. S., et al. 2022, *The Astrophysical Journal Letters*, 924, L21, doi: [10.3847/2041-8213/ac4027](https://doi.org/10.3847/2041-8213/ac4027)
- Zhao, G. Q., Meyrand, R., Feng, H. Q., Wu, D. J., & Kasper, J. C. 2022, *The Astrophysical Journal*, 938, 124, doi: [10.3847/1538-4357/ac9380](https://doi.org/10.3847/1538-4357/ac9380)
- Zhao, S., Yan, H., Liu, T. Z., Yuen, K. H., & Wang, H. 2023, arXiv e-prints, arXiv:2301.06709, doi: [10.48550/arXiv.2301.06709](https://doi.org/10.48550/arXiv.2301.06709)
- Zhdankin, V., Boldyrev, S., & Chen, C. H. K. 2016, *MNRAS*, 457, L69, doi: [10.1093/mnras/rlv208](https://doi.org/10.1093/mnras/rlv208)